PARAMETERIZATION OF MAXIMUM WAVE HEIGHTS FORCED BY HURRICANES: APPLICATION TO CORPUS CHRISTI, TEXAS

A Thesis

by

SYM ANTONNE TAYLOR

Submitted to the Office of Graduate Studies of
Texas A&M University
in partial fulfillment of the requirements for the degree of

MASTER OF SCIENCE

Approved by:

Chair of Committee,	James M. Kaihatu
Committee Members,	Francisco Olivera
	Steven F. DiMarco
Head of Department,	John Niedzwecki

December 2012

Major Subject: Ocean Engineering

ABSTRACT

In recent times, communities and structures along the Gulf of Mexico have experienced the destructive and devastating impact of hurricane surges and waves. While the impacts of surges have been studied, there exists a need for (1) the understanding of open-coast and bay environment hurricane wave conditions and (2) expedient prediction, for rapid evaluation, of wave hazards as a function of hurricane parameters. This thesis presents the coupled ADCIRC-SWAN numerical model results of wave height sensitivity based on the investigation of several hurricane parameters. Also presented is the development of parameterized maximum significant wave height models. These are determined by incorporating three forms of an equivalent fetch into (1) dimensionless best-fit equations and (2) Shoreline Protection Manual (SPM) method.

Computational results indicate that for a range of simulated hurricane parameters, a wide range of spatial and temporal characteristics, for the significant wave height, exists. The location of hurricane landfall results in a significant difference in the wave height at specified points. Additionally, the variation in central pressures, radius sizes and forward speeds leads to elevated surge levels that contribute to wave generation. Furthermore, the time evolution trend of the generation of the significant wave height is found to be unique to its geographic location.

In the development of parameterized maximum significant wave height models, the dimensionless best-fit equation approach indicates how strongly the various forms of the equivalent fetch and the bathymetric depth ultimately determines the predicted

maximum significant wave height. This approach yielded RMSE that range between 0.52m – 0.68m. Additionally, the accuracy for this approach varied greatly as the highest scatter index was 0.28 for the open-coast points and 0.37 for the bay points. The SPM approach gives an indication of how strongly the functional form of the equivalent fetch determines the predicted maximum significant wave height. When compared to the dimensionless approach, this method produced a lower RMSE of 0.37m and a greater accuracy for the scatter index of 0.23 for the open-coast points and 0.31 for the bay points.

DEDICATION

To my family and friends

ACKNOWLEDGEMENTS

First, I would like to thank my committee chair, Dr. James Kaihatu, for his support and guidance during my graduate career. I would also like to thank my thesis committee members, Dr. Francisco Olivera and Dr. Steve DiMarco, for their time, consenting to be on my committee, and contributions in reviewing this work. I am very grateful for Dr. Jennifer Irish, for allowing me to work on an aspect of this exciting project. I would like to extend a special thanks to Dr. Casey Dietrich and Dr. Celso Ferreira, for always answering my ADCIRC-SWAN troubleshooting questions that had plagued me earlier in my research career. I extend a sincere thanks and gratitude to the Organization of American States (OAS) for the generous fellowship for my graduate education at Texas A & M University. Finally, I want to thank my family and friends for all the prayers, earnest support, and unfailing love that they provided for me during my life and, especially, here. Without you, none of this would be possible.

TABLE OF CONTENTS

Page

Page

LIST OF FIGURES

Page

Page

Page

LIST OF TABLES

Page

CHAPTER I

INTRODUCTION

1.1 The Hazard of Hurricane Storm Surge and Waves

Hurricanes are one of the most deadliest, destructive and costliest forms of natural disasters known to man. In fact, the 1900 Galveston hurricane remains the deadliest natural disaster in U.S. history as it left 8,000 people dead and 3,600 buildings destroyed (NOAA, 2012). Since 2004, there have been nine major hurricanes that affected the Gulf of Mexico coastline (NOAA-NHC, 2012a). In 2005 hurricane Katrina, for example, became the most costly and third most deadly hurricane in US history, resulting in over 1800 deaths and over $80 billion in damages along the coast of the Gulf of Mexico (Knabb et al., 2005). Similarly, in 2008 hurricane Ike resulted in 64 deaths and over $10.0 billion dollars in insured damages in Texas, Louisiana, and Arkansas (Berg, 2009). Moreover, since the establishment of the Federal Emergency Management Agency (FEMA), eight hurricanes are listed as the most expensive disasters that affected the United States (FEMA, 2010a).

The disastrous effects of hurricanes are caused by four main factors: storm surges, waves, strong winds and extreme rainfall. Along the coast, storm surge is often the greatest threat to life and property. Hurricane Katrina is a prime example of the damage and devastation that can be caused by surge. At least 1500 persons lost their lives during Katrina and many of those deaths occurred directly, or indirectly, as a result of surge (NOAA-NHC, 2012b). Additionally, during this storm, surge had impacted

large segments of the population, tourism centers, oil and gas industries and key transportation arteries (Knabb et al., 2005).

Adding to the destructive power of surge, waves may increase damage to buildings directly along the coast. Water weighs approximately 1,000 kg/m^{3}00; thus, extended battering by frequent waves can damage any structure not specifically designed to withstand wave forces. The two elements work together to increase the devastating impact on land because the surge makes it possible for waves to extend inland (NOAA-NHC, 2012b). With major storms like Katrina, Camille and Hugo, devastation of coastal communities occurred. Additionally, waves, in combination with strong tidal currents, severely erode beaches and coastal highways (FEMA, 2010).

1.2 Hurricane Wave Damage

At the coast, storm surge combined with wave action has the greatest potential for extensive damage (FEMA, 2010b). Numerous reports have documented storm surge and wave related damage (Knabb et al., 2005; Padgett et al., 2008; Kraus et al., 2009; Berg, 2009; Kennedy, 2011a) from various hurricanes, thus stressing the need of the importance of accurate prediction of hurricane impacts on coastal residences and structures.

In a qualitative forensic assessment of residential damage on Bolivar during Hurricane Ike, Kennedy et al. (2011a), observed that in most shoreline areas, homes were destroyed by wave induced forcing. This damage was identified at ground level from obvious impacts to flooring systems or other damage on the seaward surface. Other

types of wave induced damages noted ranged from waves and surge destroying the house superstructure on top of pilings, to the widespread pile collapse from erosion and very high wave loads simultaneously. The authors further observed that the wave damage on surviving houses was most obvious at the immediate shorefront and decreased further inland.

The stability of coastal structures and bridges directly exposed to intensified wave forces during hurricane events are a major concern. Padgett et al. (2008), describes the observed damage patterns in a study of 45 bridges that sustained damage in Alabama, Louisiana, and Mississippi, during Hurricane Katrina. The authors observed that the most common severe failure mode for bridges were the unseating of individual spans cause by excessive motion of the bridge decks. This displacement of bridge decks is attributed primarily to the combination of the storm surge buoyant forces and battering waves lateral forces.

1.3 Thesis Content

Hurricane storm waves and surge are known to cause catastrophic damages to coastal communities and structures; thus, an understanding of these conditions is necessary in order to prepare for future events. In addition, predictions of these conditions need to be expedient to allow for rapid evaluation of hazardous storm waves and surge. As a result, we seek to assess the near shore maximum wave conditions as a function of hurricane parameters. Hence, the objectives of this research are as follows:

- Review existing deep and shallow water wave parameterized models found in literature;
- Perform simulations to determine the sensitivity of significant wave height for a range of varying hurricane parameters which includes landfall location, central pressures, radius sizes and forward speeds;
- Develop general, parameterized response models for maximum wave height as a function of hurricane parameters.

This thesis is comprised of five chapters. Chapter I identifies the threat of hurricanes surge and waves and their devastating effect on US coastlines. Chapter II presents a background overview on the governing equation for waves and surge, as well as a literature review of the existing body of research relating to parameterized wave models. Chapter III details the hydrodynamic, wave, and wind models used in the study. This chapter also outlines the numerical strategy and processes for wave height sensitivity and maximum significant wave height parameterization analyses. Chapter IV discusses and compares the results of the simulations. Chapter V presents the conclusions and recommendations for further research.

CHAPTER II

BACKGROUND AND LITERATURE REVIEW

2.1 Introduction

This chapter provides a foundation for investigating the wave height responses with respect to varying hurricane parameters and the development of maximum wave heights equations. Section 2.2 gives an introduction to the basic types of ocean waves. As maximum wave heights are accompanied by storm surge, an overview of the physics and governing equations that described storm surge and waves are discussed in Section 2.3 and Section 2.4, respectively. Section 2.5 provides an overview of the literature that describes the hurricane wave field. Empirical equations have been investigated to describe waves in deep and shallow water. Hence, Section 2.6 discussed the deep water parameterized equations that described wave heights in hurricane conditions. Section 2.7 discussed the shallow water equations to described wave heights in shallow water.

2.2 The Basic Types of Ocean Waves

In general, there are five basic types of ocean waves. Sound waves are due to water compressibility. Gravity waves are induced by gravitational forces that act on water particles displaced from equilibrium at the ocean surface. Short, high frequency capillary waves arise from the combination of the turbulent wind and surface tension at the contact surface between air and water. Planetary (or Rossby) waves are induced by

the variation of the equilibrium potential vorticity, due to changes in depth and latitude (Massel, 1996).

Ocean surface responses occupy an extraordinarily broad range of wavelengths and periods, from capillary waves, with periods of less than a second, through wind-induced waves and swell with periods on the order of a few seconds, to tidal oscillations with periods of the order of several hours and days. Figure 1 depicts the schematic representation of energy contained in the surface waves and the frequency range associated with external forces. Meanwhile, the physical mechanisms generating these waves are listed in Table 1 (Massel, 1996).

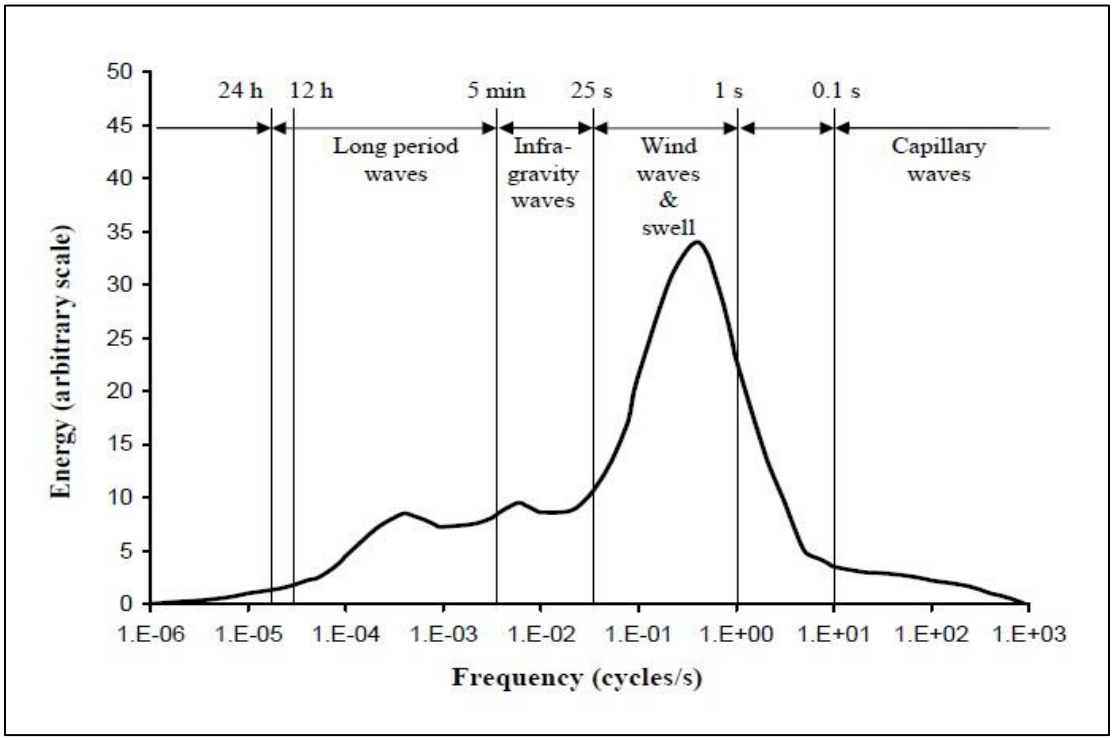

Figure 1. Schematic distribution of wave energy in frequencies (From Massel, 1996).

Table 1. Waves, physical mechanisms, and periods (From Massel, 1996).

Wave type	Wave name	Physical mechanism	Period
Capillary waves	Capillary waves	Surface tension	< 0.1 s
Wind waves & Swell	Wind waves	Wind shear, gravity	< 15 s
	Swell	Wind waves	< 30 s
Infra-gravity waves	Surf beat	Wave groups	1 - 5 min
	Seiche	Wind variation	2 - 40 min
	Harbor resonance	Surf beat	2 - 40 min
Long period waves	Tsunami	Earthquake	10 min - 2 hr
	Storm surge	Wind stresses and atmospheric pressure variation	1 -3 days
	Tides	Gravitational action of the moon and sun, earth rotation	12 - 24 hr

2.3 Governing Equations for Surges

A storm over shallow near-shore coastal waters can generate large water level fluctuations, or storm surges, if the storm is sufficiently strong and the water body is shallow over a large enough area (Sorensen, 1993). To study these conditions, it is assumed that the vertical fluid depth is much smaller than the horizontal scale of motion, a hydrostatic vertical pressure distribution exists and the fluid density is constant. Therefore, integration of the three-dimensional equations of continuity and motion through the fluid depth yields the two-dimensional shallow water equations for the conservation of mass and momentum (Lynch and Gray, 1979).

The vertically integrated continuity equation (Luettich and Westerink, 2004) becomes:

$$\frac{\partial H}{\partial t} + \frac{\partial}{\partial x}(UH) + \frac{\partial}{\partial y}(VH) = 0 \qquad (2.1)$$

where,

$U,V \equiv \frac{1}{H}\int_{-h}^{\zeta} u,v\, dz =$ depth-averaged velocities in the x, y directions,

$u,v =$ vertically-varying velocities in the x, y directions,

$H \equiv \zeta + h =$ total water depth,

$h =$ bathymetric depth,

$\zeta =$ free water surface elevation.

The vertically integrated momentum equations are:

$$\frac{\partial U}{\partial t} + U\frac{\partial U}{\partial x} + V\frac{\partial U}{\partial y} - fV = -g\frac{\partial\left[\zeta + P_s / g\rho_o - \alpha\eta\right]}{\partial x} + \frac{\tau_{sx}}{H\rho_o} - \frac{\tau_{bx}}{H\rho_o} + \frac{M_x}{H} - \frac{D_x}{H} - \frac{B_x}{H}, \tag{2.2}$$

$$\frac{\partial V}{\partial t} + U\frac{\partial V}{\partial x} + V\frac{\partial V}{\partial y} - fU = -g\frac{\partial\left[\zeta + P_s / g\rho_o - \alpha\eta\right]}{\partial y} + \frac{\tau_{sy}}{H\rho_o} - \frac{\tau_{by}}{H\rho_o} + \frac{M_y}{H} - \frac{D_y}{H} - \frac{B_y}{H}, \tag{2.3}$$

where,

$g =$ gravitational acceleration,

$D_x,\ D_y =$ momentum dispersion,

$M_x,\ M_Y =$ lateral stress gradient,

$B_x,\ B_y =$ baroclinic pressure gradient,

f = Coriolis parameter,

ρ_o = water density,

τ_{sx}, τ_{sy} = surface stresses,

τ_{bx}, τ_{by} = bottom stress components,

P_s = atmospheric pressure,

η = equilibrium tide potential,

α = effective Earth elasticity factor ($\alpha = 0.69$).

From Equation 2.2 and 2.3, the dominant forces that contribute to hurricane storm surge arise from the wind stress, the barometric pressure reduction, the Coriolis force, and the wave set-up (Dean and Dalrymple, 2002). Wind stress is created by the frictional drag of the wind blowing on the water surface and is empirically determined from

$$\tau_s = \rho c_f W^2 \tag{2.4}$$

where τ_s is the wind stress, ρ is the density of water, c_f is a dimensionless friction coefficient and W^2 is the wind speed measured at an elevation of 10m (Dean and Dalrymple, 2002). In hurricane conditions, the across shore component of wind stress increases in importance as the water depth decreases, hence winds blowing onshore over shallow water will produce a setup along the coast, and conversely. The force balance is represented by:

$$\rho g H \eta_x = \tau_w - \tau_b \tag{2.5}$$

where ρ is the water density, g is the acceleration of gravity, H is the total water depth, η_X is the across shore slope of the sea surface, τ_w is the wind stresses and τ_b is the bottom stresses (Weisberg and Zheng, 2006). Equation 2.5 shows that the across shore sea surface slope is directly proportional to the wind stress and inversely proportional to the water depth. Hence, storm surge levels along a coast are dependent on the bathymetry, with broad, shallow continental shelves more prone to large surge than narrow, deep continental shelves.

The barometric setup is the response of the coastal waters to the hurricane, and it is characterized by the elevation of the water level in the low pressure region. The magnitude of the barometric response, compared to the wind stress, is small and can be estimated as

$$\eta_B = \frac{\Delta p}{\gamma}, \tag{2.6}$$

where η_B is barometric response, Δp is the difference in pressure (from the low pressure at the center of the storm to the ambient pressure) and γ is the specific weight of water. The barometric response can be further expressed as:

$$\eta_B = 1.04\Delta p, \tag{2.7}$$

where η_B is measured in centimeters and Δp is measured in millibars (Dean and Dalrymple, 2002).

The Coriolis setup occurs when the storm forces strong currents to flow along the shoreline due to the force resulting from the earth's rotation. This component of storm

surge can be important for large currents, but it can also act to reduce storm surge when the current is flowing in the opposite direction (Dean and Dalrymple, 2002).

2.4 Governing Equations for Waves

In this study, the two most important aspects of waves are the wave set-up and radiation stresses. Under hurricane conditions wave set-up is considered an important contribution to storm surge.

When waves enter coastal waters, their amplitude and direction will be affected by the limited water depth. Additionally, a limited water depth also affects the generation, nonlinear wave-wave interactions and dissipation of wave energy. In shallow water the wave group velocity slows down, thus there is more transfer of energy from wind to waves. As a result of the combined effects of wind and a shallow water depth, the waves steepen, thus enhancing nonlinear wave-wave interactions, white-capping, and depth limited breaking. Overall, the most dominant processes that affect the waves are shoaling, refraction and depth induced breaking (Holthuijsen, 2007).

Shoaling and refraction both represent the effect of varying depth on wave height and direction. The change in wave height due to shoaling can be obtained from an energy flux balance represented by:

$$\frac{\mathrm{d}}{\mathrm{ds}}\left(c_g E\right) = 0, \tag{2.8}$$

where $c_g E$ is the energy flux per unit crest length (energy, $E = \rho_w g H^2 / 8$, for wave height H) and s is the coordinate in the direction of wave propagation. Therefore, a

decrease in group velocity, c_g, is accompanied by a corresponding increase in wave height (WMO, 1998). The change in phase velocity will turn the wave direction. This occurs as the shallow water part of the wave crest velocity is slowed down, whereas the deeper part of the crest retains its speed. This change in direction of the wave crest is governed by Snell's law, by which, along the wave ray:

$$\frac{\sin\theta}{c_{phase}} = const., \tag{2.9}$$

where the angle θ is taken between the wave ray and the normal to the depth contour. Due to refraction, the change in wave height can be represented by an energy balance:

$$\frac{\mathrm{d}}{\mathrm{ds}}\left(c_g E \cdot \Delta b\right) = 0, \tag{2.10}$$

where the energy transport, $(c_g E)$, between two adjacent wave rays, Δb, is constant (WMO, 1998).

Depth-induced breaking occurs when the crest attains a speed sufficiently high to overtake the preceding trough. One model for depth-induced wave-breaking is represented by Battjes and Janssen (1978), as described in Holthuijsen (2007):

$$D_{surf,wave} = -\frac{1}{4}\alpha_{BJ}\rho g f_0 H_{br}^2 \tag{2.11}$$

where $\alpha_{BJ} \approx 1$ is a tunable coefficient, f_0 is the inverse of the wave period, ρ is the water density, g is the gravitational constant and H_{br} is the height of the breaking wave.

As waves propagate towards the coast, the processes of generation and dissipation cause a horizontal variation in the flux of energy and momentum. The corresponding variations in momentum flux are manifest in gradients in the mean sea surface and the generation of wave driven currents (WMO, 1998). The wave momentum fluxes are proportional to the wave energy; hence, when waves break, the momentum flux decreases. This change in momentum flux is balanced by changes in the mean water level.

The onshore-directed momentum flux is the radiation stress, S_{xx}, which is defined (within in the surf zone) as:

$$S_{xx} = \frac{3}{16}\rho g \kappa^2 \left(h + \bar{\eta}\right)^2, \tag{2.12}$$

where κ is the breaking index (Dean and Dalrymple, 2002). The gradient in momentum flux is balanced by a slope in water level within the surf zone. This slope is represented by:

$$\frac{\partial \bar{\eta}}{\partial x} = -\frac{1}{\rho g \left(h + \bar{\eta}\right)} \frac{\partial S_{xx}}{\partial x}, \tag{2.13}$$

where $\bar{\eta}$ is the wave set-up. Wave set-up occurs within the wave breaking zone and results in a super-elevation of the water level. The setup is due to the transfer of wave momentum from the breaking waves to the water column.

2.5 Hurricane Wave Field

Complex ocean wave fields are generated by the large gradients in wind speed and the rapidly varying wind directions of the hurricane vortex. An understanding of these physical processes for hurricane wind wave evolution has been gained from a combination of in situ measurements at single points during the passage of hurricanes, remote sensing data and the application of numerical models (Young, 1999).

However, an advancement in the understanding of the spatial distribution of significant wave height was made by King and Shemdin (1978), who introduced the concept of an extended fetch for a translating hurricane (Young, 2003). The wave field has an even greater degree of asymmetry due to the combined influence of the asymmetry of the wind field and the extended fetch which exists within a translating hurricane. The wind vector in the intense wind region to the right of the storm center (northern hemisphere) is approximately aligned within the direction of forward propagation. Therefore, waves generated in this region tend to move forward with the hurricane and therefore remain in the high wind regions for an extended period of time. In contrast, waves generated in the low wind side of the storm (left side in northern hemisphere) propagate in the opposite direction to the hurricane translation and rapidly move away from the high wind areas. As a result, the spatial distribution of the wave field does not exactly mirror the wind field (Young, 2003). Figure 2 displays a schematic diagram of the generation of waves in a translating hurricane. Low frequency waves generated in the intense wind regions to the right of the storm center will have group velocities which are typically greater than the velocity of forward movement of

the storm, V_{fm}. Hence, these components will appear as swell ahead of the storm center. This swell radiates out from the spatially localized generation area. Hence, the spectrum ahead of the storm often consists of locally generated wind sea together with swell radiating from the center of the storm (Young, 1999).

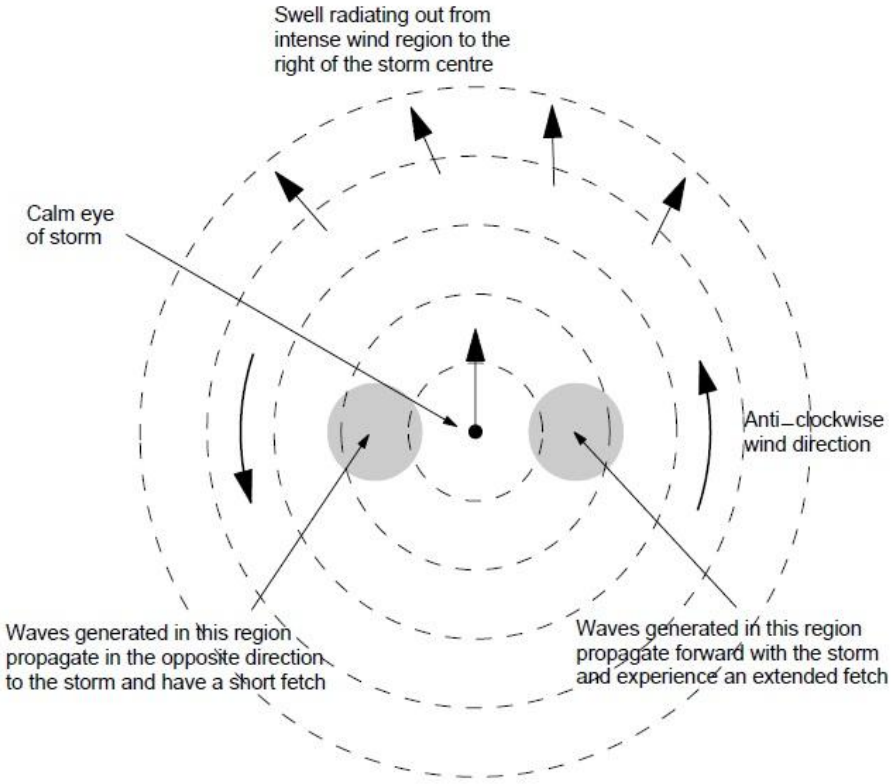

Figure 2. Schematic diagram showing the generation of waves within a translating hurricane (From Young, 2003).

An extended fetch is also important in determining the wave height within a hurricane. Not only is the wave height determined by the maximum wind speed, V_{max}, but also by the period of time the waves remain within the intense wind region. As V_{max} increases, the period of the waves generated and hence the group velocity at which they propagate also increases, as nonlinear interactions move energy to lower frequencies. Consequently, V_{fm} must also increase for the most severe wave conditions to occur. For a given value of V_{max}, the wave height could be expected to increase with increasing V_{fm} until a maximum is reached (Young, 1999).

2.6 Parameterized Wave Models

Several practical approaches are presently used for estimating maximum wave heights generated by hurricanes. The most popular consists of parametric models developed on the basis of numerical modeling of wave evolution under hurricane forcing. An example is the parametric model proposed by Young (1988), which have been widely used in hurricane forecast guidance (Kumar et al., 2003; Panigrahi et al., 2010; Wu et al., 2003). Young's (1988) model was developed from ADFA1 numerical model results, which is a second generation Sea Wave Modeling Project (SWAMP) spectral wave model based on a numerical solution of the radiative transfer equation (Young, 1988).

Young's (1988) parametric model estimates hurricane-generated maximum wave heights, $H_s^{\max}$ within a storm based on Bretschneider (1957) concept of an equivalent

fetch, X_{eq} , and the standard Hasselmann et al. (1973) JONSWAP fetch-limited growth relationship, which is expressed as:

$$\frac{gH_s}{U_{10}^2} = 0.0016\left(\frac{gX}{U_{10}^2}\right)^{0.5}, \tag{2.14}$$

where H_s is the significant wave height, U_{10}^2 is the 10m wind velocity, g is the acceleration of gravity and X is the fetch length.

An attempt to incorporate the qualitative understanding of the hurricane wave field into a quantitative model was made by Young. Young assume that the JONSWAP relationships, originally developed for fetch-limited conditions, could also be applied in hurricane wind fields with the specification of a suitable equivalent fetch. In Equation 2.14, the wind field is quasi-homogeneous and X is the downwind distance along a straight line. However, for a moving storm, Young (1988) proposed that the actual fetch be replaced by an equivalent fetch, X_{eq} . Consequently, X_{eq} should represent (i) the distance over which V_{max} effectively contributes to wave growth (no longer a straight line), and (ii) the added growth due to an extended fetch effect, resulting from waves moving forward with the storm (Alves et al., 2004). Young's (1988) modification is represented by

$$\frac{gH_s^{\max}}{V_{\max}^2} = 0.0016\left(\frac{gX_{eq}}{V_{\max}^2}\right)^{0.5}, \tag{2.15}$$

This quantity, X_{eq}, is defined as a function of three wind field parameters which ultimately determine the magnitude of $H_s^{\max}$; the forward advection velocity of the storm, V_{fm}, the maximum wind speed, V_{max}, and the radius to maximum winds, R_{max}.

In Young's parametric model, V_{fm} and V_{max} play a dual role in determining the maximum significant wave height within the storm, the spatial distribution of waves and the directional properties. The third parameter, R_{max}, acts as a nonlinear scaling parameter representing the relative size of the hurricane system. Initial X_{eq} values are determined from the JONSWAP equation by using $H_s^{\max}$ calculated from an extensive set of model simulations using a range of V_{max} and V_{fm} and fixed referenced $R_{\max}^{ref}$ of 30km. Although the model is empirical, it implicitly incorporates the consistent non-dimensional scaling of JONSWAP, together with the parameters observed to be important in determining the wave field in a hurricane (Young, 1999).

This generalized equivalent-fetch relationship from Young (1998) is in the form:

$$X_{eq} = R'\psi\left[aV_{\max}^2 + bV_{\max}V_{fm} + cV_{fm}^2 + dV_{\max} + eV_{fm} + f\right], \qquad (2.16)$$

where $a = -2.175\times10^{-3}$, $b = 1.506\times10^{-2}$, $c = -1.223\times10^{-1}$, $d = 2.190\times10^{-1}$, $e = 6.737\times10^{-1}$ and $f = 7.980\times10^{-1}$ are the polynomial coefficients determined from curve fitting.

Simulations made with other values for R_{max} that range from 15km – 60km, are then used to provide a scaling relationship for the polynomial equivalent-fetch expression. Thus, R' is a spatial scale parameter related to R through the non-linear relationship:

$$R' = 22.5\times10^3 \log R - 70.8\times10^3. \qquad (2.17)$$

The term ψ is a scaling factor which in Young (1988) was taken as 1. Later, Young (2003), based on observations or more than 100 hurricanes, redefined ψ as:

$$\psi = -0.015V_{\max} + 0.0431V_{fm} + 1.30. \tag{2.18}$$

Alves et al. (2004) noted that a major limitation of Young's parameterization for maximum hurricanes waves is the use of simulations made with a second-generation wave model. The authors argued that although his proposed parametric model may be successful in practical applications, a more refined parameterization require simulations made with a third-generation wave model. As a result, Alves et al. (2004) investigated how third-generation model simulations impact the form and structure of a parametric hurricane generated wave prediction model. In this effort, polynomial coefficients in Equation 2.16 and Equation 2.17 are re-derived by fitting V_{fm} and V_{max} to X_{eq}, estimated from $H_s^{\max}$ computed using the third generation model WAVEWATCH III. Hence, Alves et al. (2004) modified version of Young (1988) equivalent fetch is represented as:

$$X_{eq} = R'_A\left[a_A V_{\max}^2 + b_A V_{\max} V_{fm} + c_A V_{fm}^2 + d_A V_{\max} + e_A V_{fm} + f_A\right], \tag{2.19}$$

where $a_A = 5.936\times10^{-5}$, $b_A = 1.719\times10^{-2}$, $c_A = -3.479\times10^{-2}$, $d_A = 8.555\times10^{-2}$, $e_A = 1.319\times10^{-1}$ and $f_A = -5.340\times10^{-1}$. Additionally, the modified version of, R', is represented as:

$$R'_A = 29.7\times10^3 \log R - 103.7\times10^3. \tag{2.20}$$

In order to improve the original Young (1988) parametric model, Alves et al. (2004) assumed that the equivalent fetch depends directly on R_{max} and not the scaling parameter as defined in Young's (1988) model. The authors further introduced the hypothesis that X_{eq} should also depend on the group speed of dominant waves, $c_g^{\max}$. This is because, R_{max}, taken as a proxy for the wind field curvature, is assumed to be important in determining the geometry of the effective fetch in a circular wind field. Also, the effectiveness of the storm forward speed V_{fm} in developing a cumulative fetch effect will depend on $c_g^{\max}$, the speed in which the dominant wave energy is travelling. Using this concept, a new equivalent fetch definition was proposed by Alves et al. (2004) as:

$$\chi = \left[R_{\max} \left(1 + \gamma V_f / c_g^{\max} \right) \right]^{\lambda}, \tag{2.21}$$

where γ and λ are determined from curve fitting to simulated values of $H_s^{\max}$. A general formula which relates back to the JONSWAP growth curve is then defined as

$$X_{eq} = a\chi^b, \tag{2.22}$$

with *a* and *b* obtained by fitting the results of χ to the JONSWAP curve (Alves et al., 2004). Table 2 displays the curve fitted parameter values for Equations 2.21 and 2.22, which are based on the $H_s^{\max}$ obtained from both Alves et al. (2004) WAVEWATCH III model and Young's (1988) model.

Table 2. Parameter values for Equations 2.21 and 2.22 (From Alves et al., 2004).

Run data	γ	λ	a	b
Alves et al. (2004)	2.3	0.5	1106.1	0.76
Young (1988)	2.1	2.8	0.6	0.29

2.7 Deep and Shallow Water Wave Functions

One of the earliest methods of wave prediction is referred to the Sverdrup-Munk-Bretschneider (SMB) method (Sorensen, 1993). The SMB method considers a dimensional analysis of the basic deep water generated functional relationship given by

$$H_s = f(U,\ F,\ t_d, g), \tag{2.23}$$

which relates the dimensionless significant wave height to the dimensionless wind fetch and duration. This is represented as:

$$\frac{gH_s}{U^2} = f\left(\frac{gF}{U^2}, \frac{gt_d}{U}\right), \tag{2.24}$$

where H_s is the significant wave height, g is the gravitational constant, U is the wind velocity, F is the fetch length and t_d is the wind duration.

In practical applications, the four parameters F , t_d , U and g are often reduced to three by expressing the duration t_d in terms of the equivalent fetch F_{eq}. The essence here of the equivalence fetch and duration is that the wind has had the same time to transfer energy to the wave component considered. This approach is justified in that the energy of young sea states is concentrated around a sharp peak. The direction of the

peak component is equal to the wind direction and, therefore, constant, but its peak frequency f_{peak} is not. The peak frequency evolves over the duration and can be expressed as

$$F_{eq} = \int_0^t c_{g,peak}(t)\,dt, \tag{2.25}$$

where $c_{g,peak}$ is the group velocity of the evolving peak frequency and F_{eq} is the equivalent fetch (Holthuijsen, 2007). This transformation can reduce the number of parameters from four to three, thus yielding:

$$\frac{gH_s}{U^2} = f\left(\frac{gF}{U^2}\right). \tag{2.26}$$

For deep water conditions, maximum wave height, $H_s^{\max}$ are a function of maximum wind speed, V_{max} and fetch, *F*. However, in intermediate - shallow water conditions, depth is a very important factor. A limited water depth not only affects the propagation of waves but it also affects the generation, nonlinear wave -wave interactions and dissipation (Holthuijsen, 2007). The dissipation (frictional effects) at the bottom removes energy from the system. Hence, for a given wind speed, fetch, and duration the resultant significant wave height should be progressively less for decreasing water depths (Sorensen, 1993).

For a water body where wave growth predominantly occurs under intermediate/shallow water conditions Equation 2.26 is modified to

$$\frac{gH_s}{U^2} = f\left(\frac{gF}{U^2}, \frac{gd}{U^2}\right), \tag{2.27}$$

where d is the water depth (Sorensen, 1993).

One commonly used method for prediction of depth dependent waves was formulated by Bretschneider (1954), who developed relationships that considered wave energy lost due to bottom friction and percolation in the permeable sea bottom. In a subsequent study, the U. S. Army Corps of Engineers extended the Bretschneider concept based on successive approximations in which wave energy is added due to wind stress and subtracted due to bottom friction and percolation. This is presented in the *Shore Protection Manual* (U.S. Army Coastal Engineering Research Center, 1984) in the form of shallow-water forecasting curves as:

$$\frac{gH}{U_A^2} = 0.283 \tanh\left(0.53\bar{d}^{3/4}\right) \tanh\left[\frac{0.00565\bar{F}^{1/2}}{\tanh\left(0.53\bar{d}^{3/4}\right)}\right], \qquad (2.28)$$

where $\bar{d}$ is the non-dimensionalized water depth defined as:

$$\bar{d} = \frac{gd}{U_A^2},$$

and $\bar{F}$ is the non-dimensionalized fetch defined as:

$$\bar{F} = \frac{gF}{U_A^2}.$$

CHAPTER III

MODELS / NUMERICAL SIMULATION STRATEGY

3.1 Introduction

This thesis presents findings that are derived from a series of physics-based models used to estimate wind fields, wave conditions and storm surge. The principal numerical models applied in this study consists of a coupled hydrodynamic and wave model, forced by a wind field model. ADCIRC is a hydrodynamic numerical model which determines storm surge, while SWAN is a wave model that generates wind-generated waves in coastal regions. The ADCIRC and SWAN models are described in Sections 3.2 and 3.3, respectively. Section 3.4 describes the coupled model ADCIRC-SWAN model which allows the execution of both models to run sequentially in time. To obtain the wind and pressure fields required to run the coupled model, the wind field model, PBL, is described in Section 3.5. With the framework of the numerical models described, the integration of these models is described in Section 3.6. Section 3.7 details the computational mesh used in the numerical methodology, while Section 3.7.1 outlines the study area of Corpus Christi. The process to investigate the sensitivity of wave height to varying storm parameters is described in Section 3.8. Section 3.9 describes the process used to determine the parameterized maximum wave height functions.

3.2 Advanced CIRCulation Hydrodynamic Model

The hydrodynamic element model used in the coupled model is the Advanced Circulation Model (ADCIRC) (Luettich et al., 1991; Luettich and Westerink, 2004). ADCIRC is a finite element model capable of resolving water surface elevations and velocities under various forcing conditions. These forcings can include wind and pressure fields, tidal constituents, wave radiation stress and user-specified boundary conditions. A grid structure consisting of nodes and triangular elements provides the framework for computations in a spherical coordinate system. As a basis for computations, ADCIRC uses a finite element scheme in space and a finite difference method in time to solve the Generalized Wave Continuity Equation (GWCE).

The GWCE is generated by combining the spatially differentiated momentum equations (Equations 2.2 and 2.3) in its conservative form with the temporally differentiated continuity equation (Equation 2.1). The finite element solution is implemented using Lagrange linear finite elements in space and three and two level schemes in time for the GWCE and momentum equations, respectively (USACE, 2011). During execution of ADCIRC, the GWCE and the momentum equations are solved sequentially, yielding the free surface elevation and depth-average velocity (Luettich and Westerink, 2004).

In this study, the Planetary Boundary Layer (PBL) model solves the governing equations for wind and provides the meteorological forcing to ADCIRC. The wind surface stress is computed from the wind velocity by a standard quadratic drag law:

$$\frac{\tau_{sx}}{\rho_o} = C_d \frac{\rho_{air}}{\rho_o} |W_{10}| W_{10-x}, \tag{3.1}$$

$$\frac{\tau_{sy}}{\rho_o} = C_d \frac{\rho_{air}}{\rho_o} |W_{10}| W_{10-y}, \tag{3.2}$$

where W_{10} is the wind speed sampled at 10-m height over a 10-min time period and the ratio of the air density to that of water, ρ_{air} / ρ_o, is 0.001293 (Westerink et al., 2008). The drag coefficient, C_d, is defined by Garratt's drag formula (Garratt, 1977):

$$C_d = (0.75 + 0.067 W_{10}) \times 10^{-3}. \tag{3.3}$$

Parallel processing techniques are used to run the ADCIRC model on distributed memory processors. Domain decomposition is employed to divide the computational mesh into portions that can be solved on individual processors (USACE, 2011). In this way, wall clock time is saved to complete the total simulation.

ADCIRC can be executed in either three dimensional or two dimensional (depth-integrated) modes. The coupled model used in this thesis involves the two-dimensional (depth integrated) form, commonly referred to as ADCIRC-2DDI (Version 29.14). ADCIRC-2DDI is widely used in the industry, academia (Atkinson et al., 2008; Bender et al., 2010; Sheppard et al., 2007), and by the Army Corps of Engineers (USACE, 2008; USACE, 2011) in the analysis of hurricane storm surge risk and development of storm protection plans.

3.3 Simulating Waves Nearshore (SWAN)

The wave model used in the coupled model is Simulating Waves Nearshore (SWAN). SWAN is a third generation wave model developed at the Technical University of Delft in the Netherlands and has been used to simulate waves in shallow water (Booij et al., 1999; Ris et al., 1999).

In SWAN, the waves are described with the two-dimensional wave action density spectrum, $N(\sigma,\theta)$, where σ is the relative frequency, θ is the wave direction. Wave action is used since it is the conserved quantity in wave-current interaction (Bretherton & Garrett, 1969). The evolution of the wave spectrum is described by the spectral action balance equation (Booij et al., 1999):

$$\frac{\partial N}{\partial t}+\frac{\partial(c_x N)}{\partial x}+\frac{\partial(c_y N)}{\partial y}+\frac{\partial(c_\sigma N)}{\partial \sigma}+\frac{\partial(c_\theta N)}{\partial \theta}=\frac{S}{\sigma}. \tag{3.4}$$

The first term on the left-hand side represents the local rate of change of action density in time, the second and third term represent propagation of action in geographical space. The fourth term represents shifting of the relative frequency due to variations in depth and currents, and the fifth term represents depth-induced and current induced refraction. The source term, S, represents the effects of generation, dissipation, and nonlinear wave-wave interactions.

The source term, S, consists of both deep and shallow water wave effects which can be represented as:

$$S_{tot}=S_{in}+S_{wc}+S_{nl4}+S_{bot}+S_{brk}+S_{nl3} \tag{3.5}$$

Deep water effects are represented by the first three terms on the right hand side of the equation. These are defined as the transfer of energy from wind to the waves, S_{in}, the dissipation of wave energy due to whitecapping, S_{wc}, and the nonlinear transfer of wave energy due to quadruplet interaction, S_{nl4}. In shallow water additional terms include: dissipation due to bottom friction, S_{bot}; depth-induced breaking, S_{brk}; and nonlinear triad interaction, S_{nl3} (Zijlema, 2010). SWAN formulations of these terms are extensively discussed in Booij et al. (1999) and Holthuijsen (2007).

Recently, SWAN has been developed for unstructured meshes, similar to that used by ADCIRC (Zijlema, 2010). This version computes the wave action density spectrum $N\left(\vec{x},t,\sigma,\theta\right)$ at the vertices of an unstructured triangular mesh, and it orders the mesh vertices so it can sweep through them and update the action density using information from neighboring vertices. It then sweeps through the mesh in opposite directions until the wave energy has propagated sufficiently through geographical space in all directions (Dietrich et al., 2011a).

3.4 ADCIRC-SWAN Coupled Model

The numerical simulations in this thesis have been performed using the coupled ADCIRC and SWAN. ADCIRC-SWAN have been integrated and coupled so that they run on the same global unstructured grid, share parallel computing infrastructure and run sequentially in time (Dietrich et al., 2011a).

The ADCIRC model is driven partly by radiation stress gradients that are computed using information from SWAN. These gradients, $\tau_{s,waves}$, are computed by:

$$\tau_{sx,waves} = -\frac{\partial S_{xx}}{\partial x} - \frac{\partial S_{xy}}{\partial y}, \tag{3.6}$$

$$\tau_{sy,waves} = -\frac{\partial S_{xy}}{\partial x} - \frac{\partial S_{yy}}{\partial y}, \tag{3.7}$$

where S_{xx}, S_{xy}, and S_{yy} are the wave radiation stresses:

$$S_{xx} = \rho_0 g \iiint \left(\left(n\cos^2\theta + n - \frac{1}{2} \right) \sigma N \right) d\sigma d\theta, \tag{3.8}$$

$$S_{xy} = \rho_0 g \iint \left(n \sin\theta \cos\theta \sigma N \right) d\sigma d\theta, \tag{3.9}$$

and

$$S_{yy} = \rho_0 g \iiint \left(\left(n\sin^2\theta + n - \frac{1}{2} \right) \sigma N \right) d\sigma d\theta, \tag{3.10}$$

where n is the ratio of group velocity to phase velocity (Dietrich et al., 2011a). The radiation stresses are computed at the mesh nodes using Equations 3.8 - 3.10, then they are differentiated to obtain the gradients in Equations 3.6 - 3.7.

The coupled model, ADCIRC – SWAN, is run in series on the same local mesh and processor. On each coupling interval, ADCIRC is executed first, since in the near-shore coastal environment wave properties are more dependent on circulation characteristics. At the beginning of a coupling interval, ADCIRC has access to the radiation stress gradients, $\tau_{s,waves}$, computed by SWAN at times corresponding to the

beginning and end of the previous interval. ADCIRC uses that information to extrapolate the gradients at all of its time steps in the current interval. These extrapolated gradients are used to force the ADCIRC solution as previously described in Section 3.2. Once the ADCIRC stage is finished, SWAN is run for one time step, to bring it to the same time as ADCIRC. SWAN has access to the wind speeds, water levels and currents computed at the mesh nodes by ADCIRC, at time beginning and end of the current interval. SWAN applies the temporal mean of those values to force its solution on its time step. Hence, the radiation stress gradients used by ADCIRC are always extrapolated forward in time, while the wind speeds, water levels, used by SWAN are always averaged over each of its time steps (Dietrich et al., 2011a). The coupled model has been validated in the hindcasts of Hurricanes Katrina, Rita (Bunya et al., 2010; Dietrich et al., 2010a; Dietrich et al., 2011a) and Gustav (Dietrich et al., 2010b).

3.5 Planetary Boundary Layer (PBL)

The forcing used in the simulations were hurricane wind and pressure fields, generated by the Planetary Boundary Layer (PBL) model of Thompson and Cardone (1996). This PBL model is derived from the vertically averaged, horizontal equations of motion formulated with respect to a moving Cartesian coordinate system, with its origin at the center of the eye (Cardone et al., 1992). These equations are represented by (Vickery et al., 2000):

$$\frac{dV}{dt} + f\left|k \times V\right| = -\frac{1}{\rho}\nabla p + \nabla \cdot \left(K_H \nabla V\right) - \frac{C_D}{h}\left|V\right|V \qquad (3.11)$$

and

$$\frac{d}{dt} = \frac{\partial}{\partial t} + V \cdot \nabla, \tag{3.12}$$

where

V = vertically averaged horizontal velocity,

f = Coriolis parameter,

k = unit vector in the vertical direction,

ρ = air density,

p = atmospheric pressure,

K_H = horizontal eddy viscosity coefficient,

C_D = drag coefficient,

h = height of the PBL.

The vertically integrated momentum flux is related to the surface stress, and the wind and pressure fields are represented in terms of hurricane parameters including central pressure (cp), storm size (Rp), storm forward speed (v_f), and peakedness (B) (Holland, 1980). The properties of these hurricane parameters are specified at one-hour intervals and the PBL model computes the wind velocities and pressures in a fifteen minute time step.

The PBL model simulates the tropical cyclone in steady state as a snapshot centered at the storm's eye. This is because hurricane structures change relatively slowly in time, whereas its location does not. Thus, a series of snapshots are computed sequentially to describe the different phases of the storm's evolution, and the

intermediate transitions between phases. The final wind and pressure fields are produced on a regular 0.05-degree by 0.05-degree grid with snapshots every 15 minutes (USACE, 2011). The pressure field is generally described as (Cardone et al., 1994):

$$p(r) = p_0 + \Delta p\, e^{-\left(\frac{R_p}{r}\right)B} \tag{3.13}$$

where

p_0 = central pressure at eye,

Δp = pressure deficit between eye and far field,

R_p = scaling radius,

r = radius,

B = constant in the general range 0.5 – 2.5.

The PBL model uses a moving coordinate system so the origin of a nested grid always coincides with the center of the hurricane. This nested – computational domain consists of a system of rectangular grids which provides relatively fine grid spacing near the hurricane inner regions and coarse spacing in the outer region. The nested domain is obtained by using seven grids with linearly increasing grid spacing (1.25km, 2.5km, 5km, 10km, 20km, 40km, and 80km) from the origin of the coordinate system. (Thompson and Cardone, 1996). The PBL model computes the wind velocities and pressure at these nested grid points at specified time steps.

3.6 Overview of Procedure

The first step was to run the parameterized PBL model using input tropical cyclone (storm trop) files, which are files that contain hourly snapshots of the storm parameters for its entire duration. The parameters included in the storm trop file, that are obtained from the storm track file, are the latitude, longitude, central pressure, storm size, storm forward speed, and Holland peakedness of the storm center. In addition to the parameters contained in the track file, the storm trop file contains other storm parameters, specified at one-hour intervals, including the storm rotation, direction, far-field pressure, steering flow and direction of steering flow. The storm trop file is used as the input file into PBL model which computes the wind velocities and pressures with a fifteen minute time step. The resulting output files are in a format compatible to ADCIRC-SWAN specification so the PBL output is directly used as wind and pressure field input forcing for ADCIRC-SWAN computation.

In addition to these meteorological forcing files, the ADCIRC–SWAN model uses five main input files. These include the unstructured finite element mesh and bathymetry file, the numerical parameter and boundary condition file, nodal attributes file, meteorological forcing input file, and the SWAN input file. The grid is defined by node numbers and locations, element neighbors and boundary information. The input parameters include the time step, duration of model run, coordinate system definitions, output parameters, and various input file parameters.

During execution of the coupled model, ADCIRC interpolates spatially and temporally to project the meteorological fields to the nodes on the unstructured mesh,

and then passes the wind velocities, water levels and currents to SWAN through processor memory. SWAN, in turn, uses those quantities to force its wave computations and all related wave processes. At the end of each time step, SWAN computes the gradients of wave radiation stress, which are then passed as a forcing function to ADCIRC (Dietrich et al., 2011a; Dietrich et al., 2011b).

At the completion of the simulation the output files specified were the global elevation time series, maximum elevation, maximum radiation stresses, maximum wind velocity, global wind velocity time series, global wave height time series, and maximum wave height. The data in these files are discussed further in this thesis. Figure 3 depicts the process used in modeling the results presented in this thesis.

The simulations are performed on the high-performance EOS computing platform. EOS is an IBM iDataplex cluster located at the Texas A & M University Supercomputing Facility (2012), and is comprised of 372 nodes and 3168 quad-core processors (2.8 GHz, 64-bit). The normal mode of problem solving on EOS is running distributed or parallel computations under the control of a batch scheduler. For parallel computations, EOS is integrated well with Message Passing Interface (MPI) as a standardized environment. For maximum efficiency, ADCIRC-SWAN simulations are performed on multiple processors (256 or 320). The coupled model uses the METIS domain-decomposition algorithm (Dietrich et al., 2011a) to decompose the mesh grid and related input files into local sub-meshes, assigning each sub-mesh to a core processor.

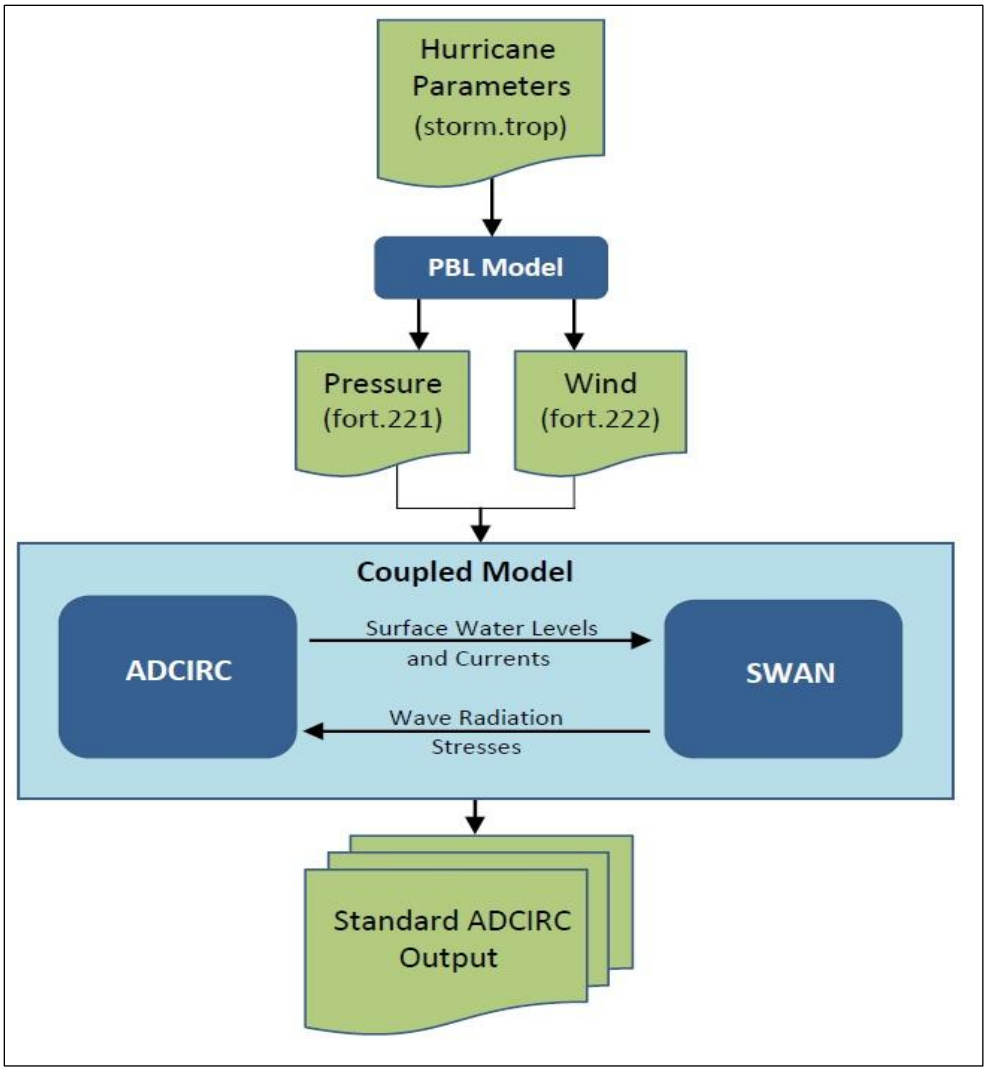

Figure 3. Overview of the numerical modeling process.

3.7 Computational Domain

The coupled model computational domain used in the simulations is derived from the TX2008 grid (USACE, 2008; Kennedy et al., 2011c) and it is an evolution of

an earlier east coast domain of Westerink et al., (1994). The grid contains 1,271,582 nodes and 2,523,296 elements. The geographical domain, shown in Figure 4, includes the Western North Atlantic Ocean, the Caribbean Sea, and the Gulf of Mexico. The east coast offshore boundary is along the 60°W meridian, which extends from Glace Bay to eastern Venezuela. Other boundaries are defined by the eastern coastlines of North, Central and South America. The topography and bathymetry within the domain, shown in Figure 5, includes the continental shelf, the continental slope, the continental rise and deep ocean.

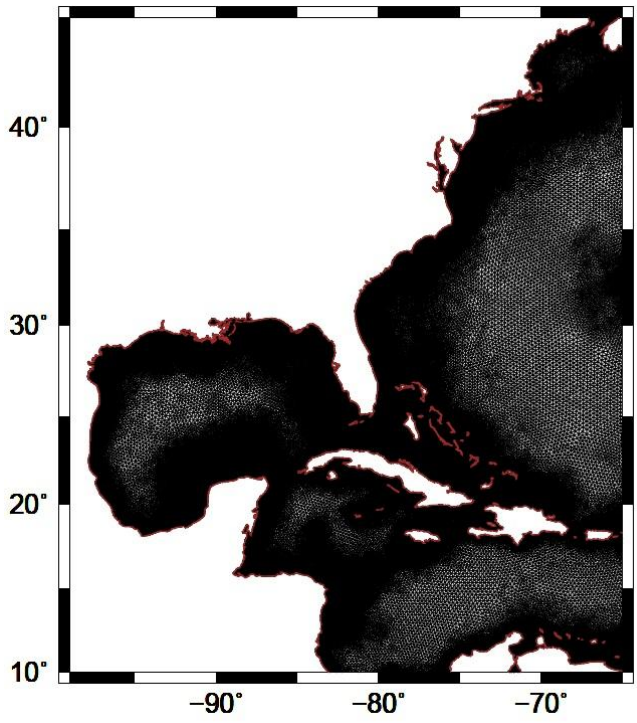

Figure 4. Computational domain extents.

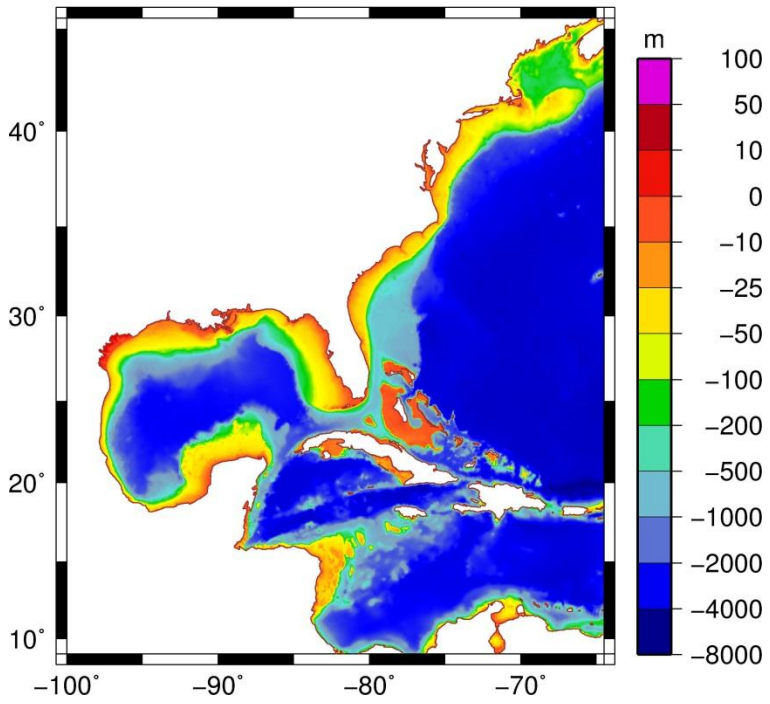

Figure 5. Computational domain bathymetry and topography.

3.7.1 Computational Domain – Corpus Christi

One of the locations used for simulation in this study is the Corpus Christi Bay (Figure 6), located near the city of Corpus Christi, Texas, on the Gulf of Mexico. It is located on the tip on southern Texas, along Corpus Christi Bay, and also includes a number of barrier islands, namely Mustang Island and the northern section of Padre Island.

The bathymetric and topographic elevations are shown in Figures 6 and 7, with depths ranging from 100m in the Gulf of Mexico to 20m elevation on the mainland. The unstructured grid mesh size is shown in Figure 8, with the variation of the larger elements in deep water to the refined areas around coastal Texas.

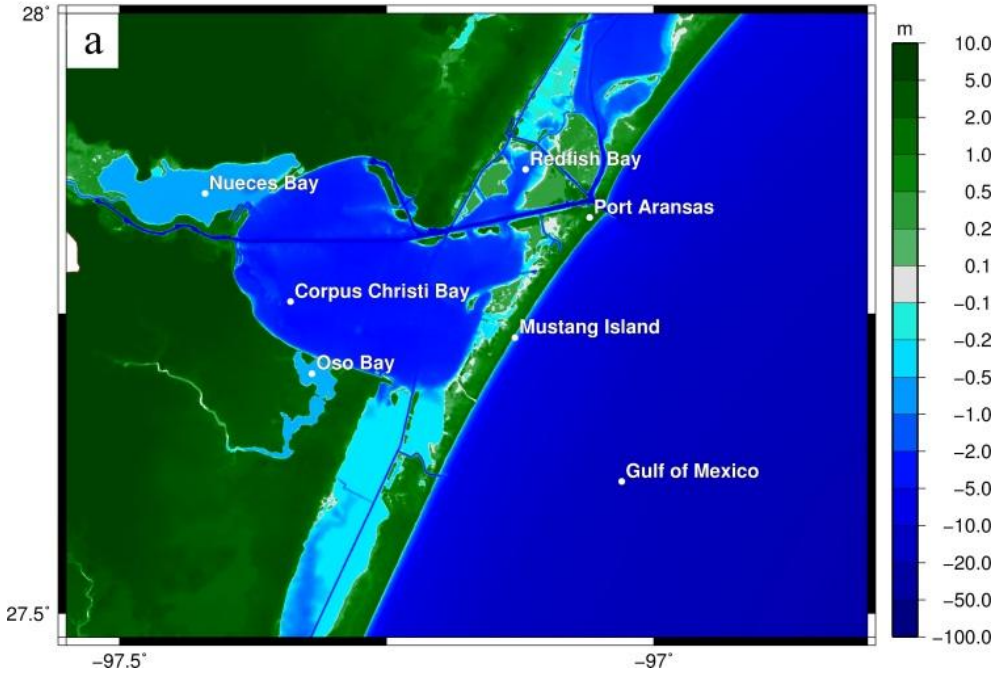

Figure 6. Map of Corpus Christi, Texas.

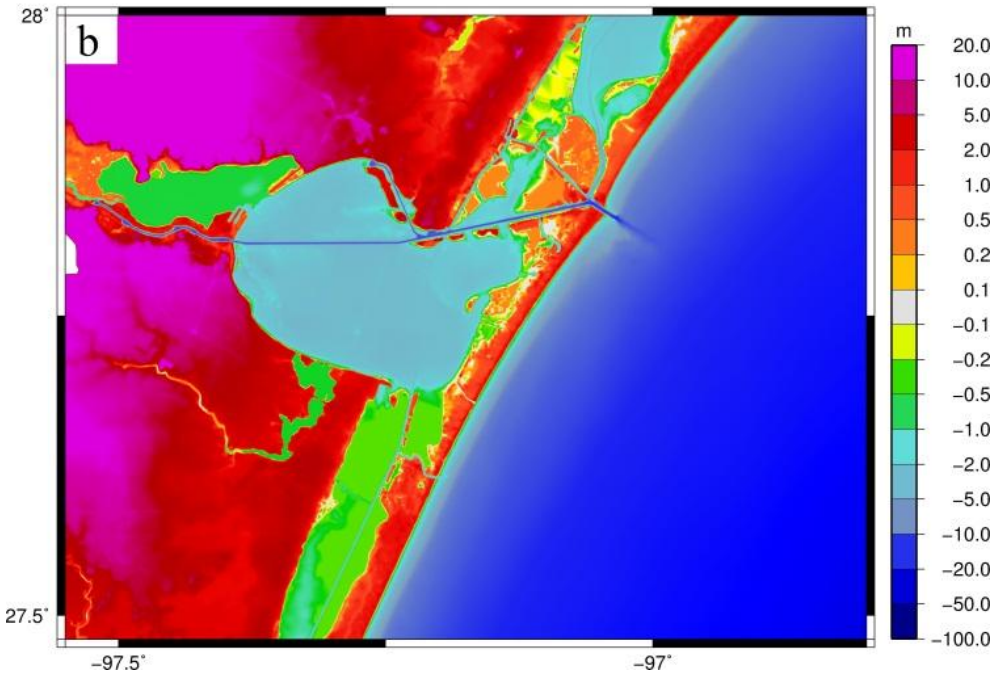

Figure 7. Mesh bathymetry and topography

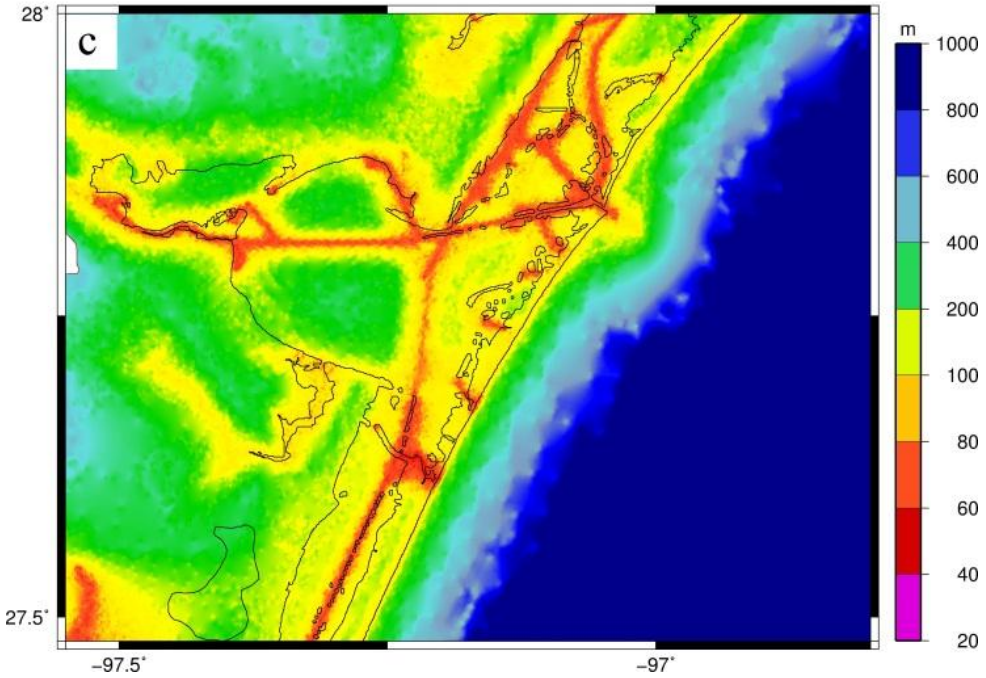

Figure 8. Mesh resolution and element sizes

Specified output locations are displayed in Figure 9, and the corresponding geographical information is listed in Table 3.

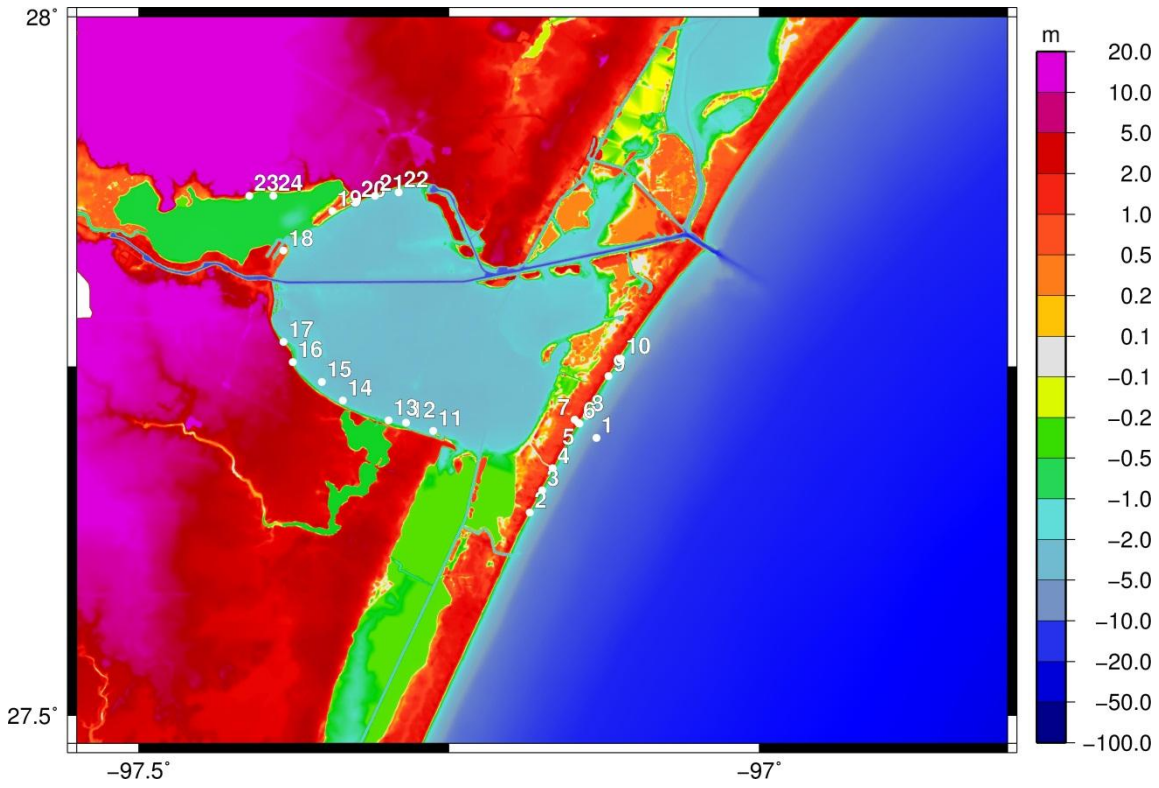

Figure 9. Output points location.

Table 3. Geographic information of output points shown in Figure 9.

Point No.	Location	Longitude	Latitude	Depth (m)	Node No.
1	Nearshore	-97.1314	27.6989	9.76	256766
2	Shoreline west	-97.1851	27.6453	0.13	288584
3	Shoreline west	-97.1751	27.6612	0.58	285325
4	Shoreline west	-97.1667	27.6771	0.15	295113
5	Shoreline	-97.1450	27.7090	0.49	285395
6	Dune	-97.1458	27.7096	-0.75	291932
7	Inland	-97.1489	27.7119	-1.15	301485
8	Shoreline east	-97.1391	27.7147	1.13	282119
9	Shoreline east	-97.1216	27.7432	0.21	288724
10	Shoreline east	-97.1115	27.7557	0.77	285452
11	Corpus Christi Bay	-97.2629	27.7039	3.34	614911
12	Corpus Christi Bay	-97.2847	27.7097	3.61	656189
13	Corpus Christi Bay	-97.2989	27.7114	2.43	673680
14	Corpus Christi Bay	-97.3357	27.7256	3.52	722000
15	Corpus Christi Bay	-97.3524	27.7390	3.91	734340
16	Corpus Christi Bay	-97.3758	27.7532	-0.94	761696
17	Corpus Christi	-97.3834	27.7674	0.13	776729
18	Corpus Christi Bay	-97.3834	27.8327	-0.42	919510
19	Corpus Christi Bay	-97.3441	27.8611	-0.08	859743
20	Corpus Christi Bay	-97.3248	27.8678	-0.13	843234
21	Corpus Christi Bay	-97.3098	27.8721	1.34	836574
22	Corpus Christi Bay	-97.2905	27.8745	3.63	833254
23	Nueces Bay	-97.4110	27.8720	0.13	959713
24	Nueces Bay	-97.3917	27.8720	0.69	942774

3.8 Model Setup for Wave Height Sensitivity Analysis

To investigate wave height sensitivity to hurricane parameters, twelve scenarios that varied hurricane sizes and central pressures are selected for simulations. Listed in Table 4, are the hurricane scenarios which have minimum central pressures between 900mb - 930mb, storm radii between 20.4km - 66.0km, and forward speeds between 2.8m/s – 11.1m/s. The sensitivity analysis assumes that, by varying one of the hurricane's parameter while keeping the others constant, wave height sensitivities are observed with respect to the varied parameter. The use of multiple storms having varying characteristics provides insight into wave height elevation changes during a range of storm conditions.

Table 4. Suite of storms used in sensitivity analysis.

Hurricane Sensitivity Parameter	Storm	Forward speed (m/s)	Storm radius (km)	Central pressure (mb)
Location	cc14-1	5.7	38.9	900
	cc15-4	5.7	38.9	900
	cc16-5	5.7	38.9	900
Pressure	cc1	5.7	20.4	960
	cc10	5.7	20.4	930
	cc11	5.7	20.4	900
Radius	`cc11	5.7	20.4	900
	cc9	5.7	40.4	900
	cc13	5.7	66.0	900
Forward speed	cc17	2.8	38.9	900
	cc14	5.7	38.9	900
	cc18	11.1	38.9	900

The first parameter investigated was hurricane landfall location as depicted by the three tracks in Figure 10. The baseline track is track 1, which originates in the Gulf of Mexico and is orientated in a northwesterly direction. The comparative tracks are track 4 and track 5, which are located 30 km south and north, respectively, of track 1. The modeled hurricanes; cc14-1, cc15-4 and cc16-5, simulated on these tracks have a forward speed of 5.7 m/s, radius of 38.9 and central pressure of 900mb.

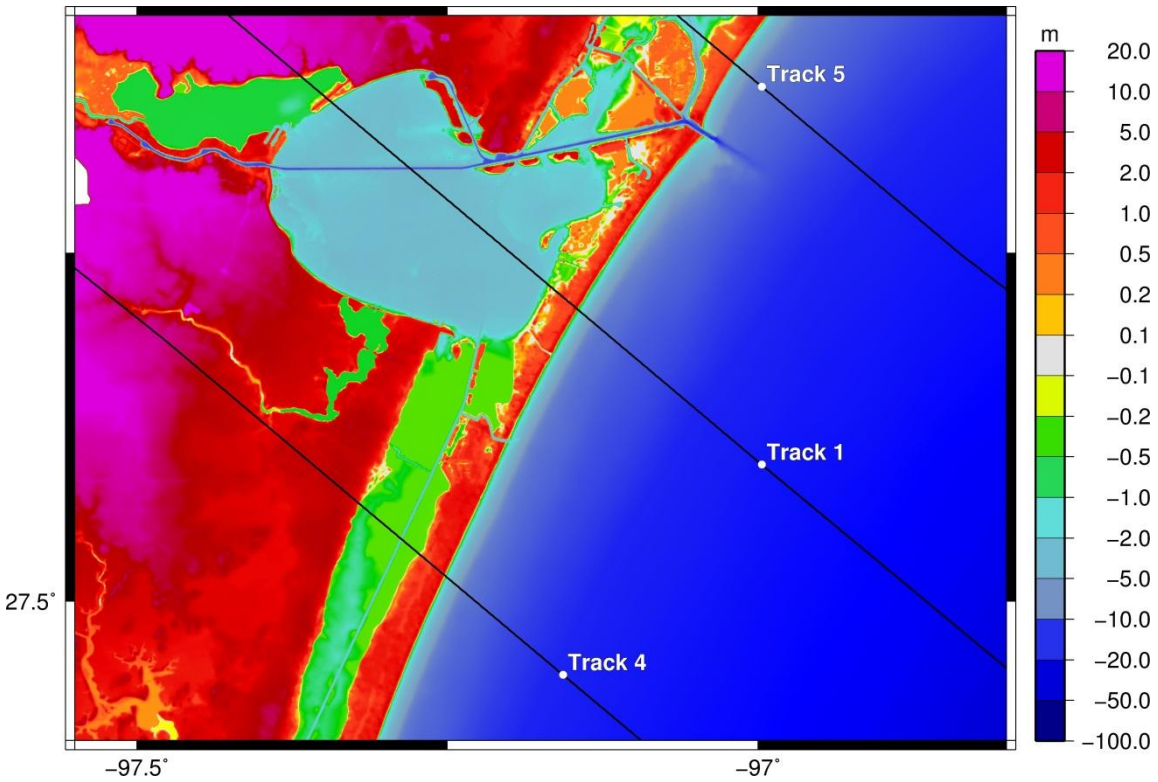

Figure 10. Location and orientation of hurricane's tracklines.

The second parameter investigated was the intensity of the hurricane. The forward speed of 5.7 m/s and the radius of 20.4 km were kept constant, and the central pressures were varied in 30mn increments from 900mb to 960mb. These simulations were performed on track 1. The third parameter investigated was the radius of the hurricane. The hurricanes modeled in this approach had a constant forward speed of 5.7 m/s and central pressure of 900mb, but the radius varied from 20.4km to 66.0km. The last parameter investigated was the forward speed of the hurricane. While the radius of 38.9km and the central pressure of 900mb were kept constant, the forward speeds 2.8m/s, 5.7m/s and 11.1m/s were simulated.

3.9 Model Setup to Determine $H_s^{\max}$ Parameterized Functions

To generate a range of near-shore wave conditions for the development of parameterized $H_s^{\max}$ functions, thirteen storms of varying central pressures and sizes are created to use on the computational grid. The properties for the storm size (Rp) and intensities (cp) were specified based on the investigation of the discrete data set of U.S. Army Corps of Engineers (2008, 2011) and Irish and Resio (2009). Accordingly, synthetic hurricane wind and central pressure fields were created (via the PBL model) with central pressures between 960mb and 900mb, and radius to maximum wind sizes between 11km and 65 km. Table 5 lists the combination of hurricane sizes and central pressures selected for this study. With this forcing, simulations are performed with the coupled ADCIRC-SWAN model to generate wave fields, surge levels, and wind

velocities as output. The outputs from these simulations are use as the parameter inputs in the development of parameterized $H_s^{\max}$ functions.

As discussed previously in Section 2.7, hurricane deep water $H_s^{\max}$ models are functions of wind speed $(V_{\max})$ and fetch (F). However, the fetch parameter would be replaced with the equivalent fetch (X_{eq}) definition as presented by Young (1988, 2003) and Alves et al. (2004). To obtain a $H_s^{\max}$ form that is similar to both Young's (Equation 2.15) and the functional form of Equation 2.26, the two dimensionless functions of $H_s^{\max}$ and equivalent fetch (X_{eq}) are graphed, and the best-fit power trend line as a function $H_s^{\max}$ is obtained. The $H_s^{\max}$ calculated from this power trend line is then graphed with the $H_s^{\max}$ outputs from the coupled ADCIRC-SWAN model, to determine the best suited functional form of Equation 2.26 and (X_{eq}) combination that can be applied for a particular coastal setting location.

For quantitative evaluation of these methods efficiency, the scatter index (SI) and the bias parameter have been used for comparison of modeled and predicted $H_s^{\max}$ values:

$$SI = \frac{\sqrt{\frac{1}{N}\sum_{i=1}^{N}(O_i - S_i)^2}}{\frac{1}{N}\sum_{i=1}^{N} O_i}, \tag{3.14}$$

$$Bias = \frac{1}{N}\sum_{i=1}^{N}(O_i - S_i), \tag{3.15}$$

where N is the total number of data, O_i is the predicted $H_s^{\max}$ value and S_i is the modeled $H_s^{\max}$ value.

Additionally, the use of the X_{eq}, as presented by Young (1988, 2003) and Alves et al. (2004), in the SPM model (Equation 2.28) is investigated. In this instance, the X_{eq} is converted into dimensionless form and replaces the dimensionless fetch parameter. The resulting $H_s^{\max}$ calculated from the combined SPM-X_{eq} method is then graphed against the $H_s^{\max}$ outputs from the coupled ADCIRC-SWAN model.

Table 5. Suite of storms used in parameterization function development.

Storm	Forward speed (m/s)	Storm radius (km)	Central pressure (mb)
cc1	5.7	20.4	960
cc2	5.7	38.9	960
cc3	5.7	66.0	960
cc4	5.7	14.8	930
cc5	5.7	32.8	930
cc6	5.7	47.8	930
cc7	5.7	11.1	900
cc8	5.7	27.6	900
cc9	5.7	40.4	900
cc10	5.7	20.4	930
cc11	5.7	20.4	900
cc12	5.7	66.0	930
cc13	5.7	66.0	900

CHAPTER IV

RESULTS

4.1 Introduction

This chapter presents the coupled ADCIRC-SWAN numerical model results. Sections 4.2 – 4.5, discuss wave height sensitivity based on the investigation of hurricane's landfall location, intensity, radius size and forward approach speed. Section 4.6 discusses the conclusions of the sensitivity analyses. Section 4.7 discuss the development of $H_s^{\max}$ models, which is determined by incorporating Young's X_{eq}, Alves's modified version of Young's X_{eq} and Alves's X_{eq} models into (1) dimensionless best-fit equations and (2) SPM model. The conclusions of the $H_s^{\max}$ model results are discussed in Section 4.8.

4.2 Sensitivity to Landfall Location

In this analysis, the baseline track to which simulations are compared is Track 1 (Figure 10), which orients from the southeast to the northwest. The modeled hurricane on this track has a central pressure of 900mb, radius of 38.9 km and a forward speed of 5.7 m/s. Planar view elevation snapshots taken at different times in the simulation are shown in Figure 11. These time frames depicts both the significant wave heights and wind velocity vectors, in relation to the hurricane location, as it approaches and passes the bay at 6 hours before landfall, at landfall, and at 6 hours after landfall. The time stamp includes an arbitrary year and uses the Universal Time Coordinated (UTC) system.

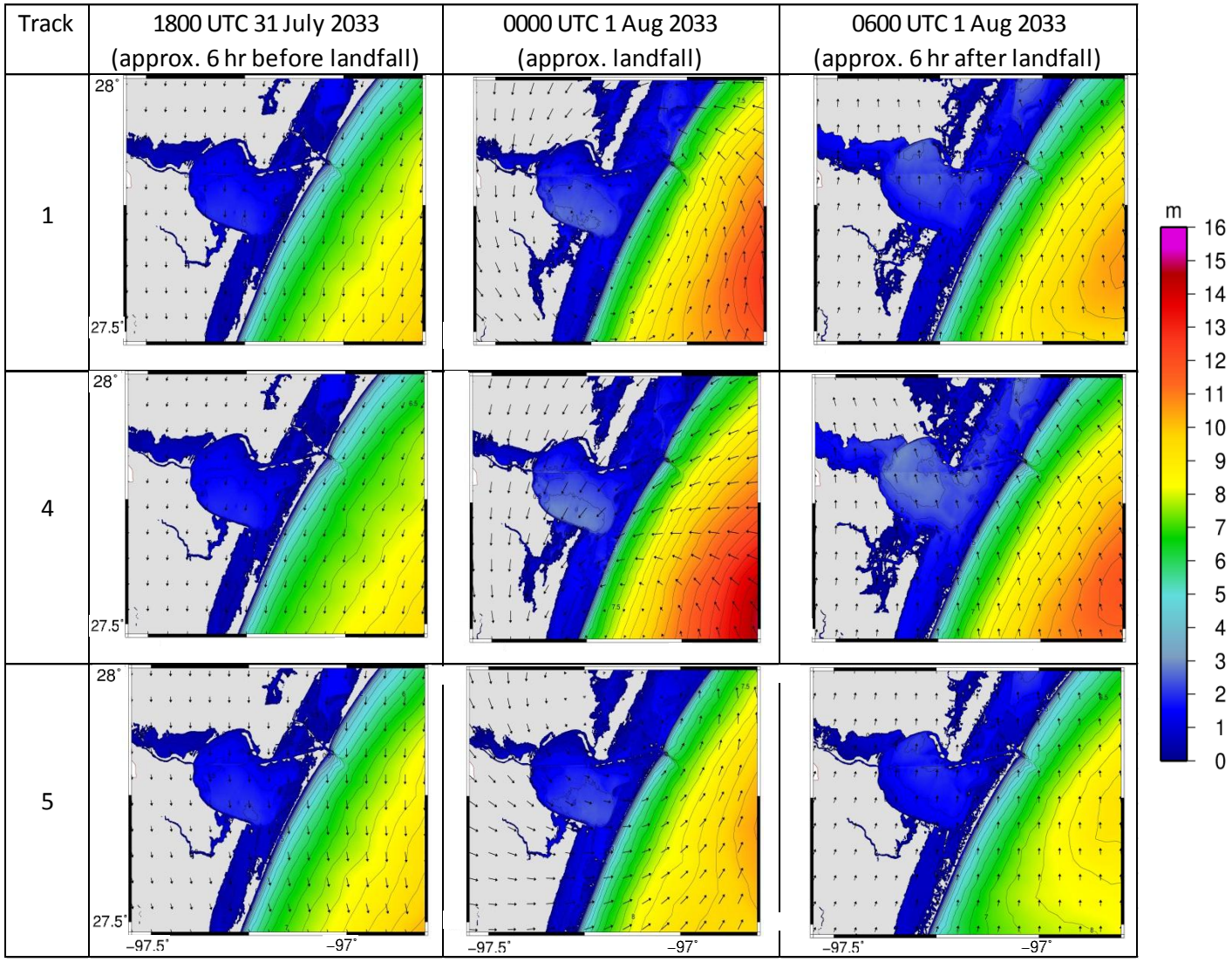

Figure 11. Results depicting sensitivity of wave heights to hurricane landfall location. Plots depicts planar view of model-simulated significant wave height contours (m) and wind vectors (m/s) snapshots at 6 hours before landfall, approximately landfall, and 6 hours after landfall. Rows represents the specified hurricane track.

On track 1, at 6 hours before landfall, the waves along the shoreline are on the order of a few meters since a southerly, alongshore-directed wind stress begins to affect the coast. At landfall, the winds to the right of the storm shift to onshore and flooding has occurred on Mustang Island, located immediately in front of the bay. Inside the bay, the waves generated are due to a complex interaction of localized hurricane winds and barrier surge inundation. After landfall and as the storm continues northwest the winds over the bay reverses direction, resulting in higher wave heights in the northern section of the bay. At 6 hours after landfall, with the winds directed onshore and northward, there exists continued generation of waves in the near-shore environment.

On track 4, at 6 hours before landfall, the hurricane waves activity is similar to that of Track 1. At landfall, the intense winds to the right of the storm are directed onshore and the wave heights are near maximum in the near-shore environment. Furthermore, due to the southern landfall location of this storm, larger wind velocity vectors in the bay generated the maximum wave heights when compared to the other tracks and landfall locations. At 6 hours after landfall, wave activity continues inside the bay as maximum wave heights, of around 3m, are seen. This is due to the fetch distance, from the southern mouth of the bay to the northern extent of the bay, over which the wind velocity vectors can generate these maximum wave heights. Additionally, waves are generated in the flooded areas of the adjacent Oso, Nueces and Redfish Bays. In the immediate near-shore environment, the hurricane's outmost winds are directed onshore and northward, and generate maximum wave heights, which range between 3m - 7m, even after the passing of the hurricane.

On track 5, at 6 hours before landfall, the hurricane waves activity are, also, similar to that of Track 1. The hurricane on this track makes landfall at a location to the north of the bay, hence the weaker wind velocity vectors are directed offshore; thus maximum wave heights in the bay are located near the entrance. Additionally, wave heights near the shoreline are much lower compared to the same time period on Tracks 1 and 4. At 6 hours after landfall, due to the northward direction of the wind velocity vectors, the maximum wave height in the bay are located at the northern extent. Also, when compared to the previous tracks, the surrounding bays are not as flooded and the wave heights in the near-shore environment are much smaller due to the weaker outmost winds.

Time series of the model-simulated wave heights at the near-shore, shoreline and Corpus Christi locations are shown in Figure 12. In the near-shore environment, the graphs have similar shapes and trends and shows that for the simulated hurricane scenario, wave generation and maximum wave height is dependent on storm landfall location. Due to its southern landfall location, the most intense winds of the storm on track 4, generated maximum wave heights at landfall that were 11.4% higher in the near-shore, 29.3% higher at the shoreline, and 55.6% higher in the bay, than the storm on track 1.

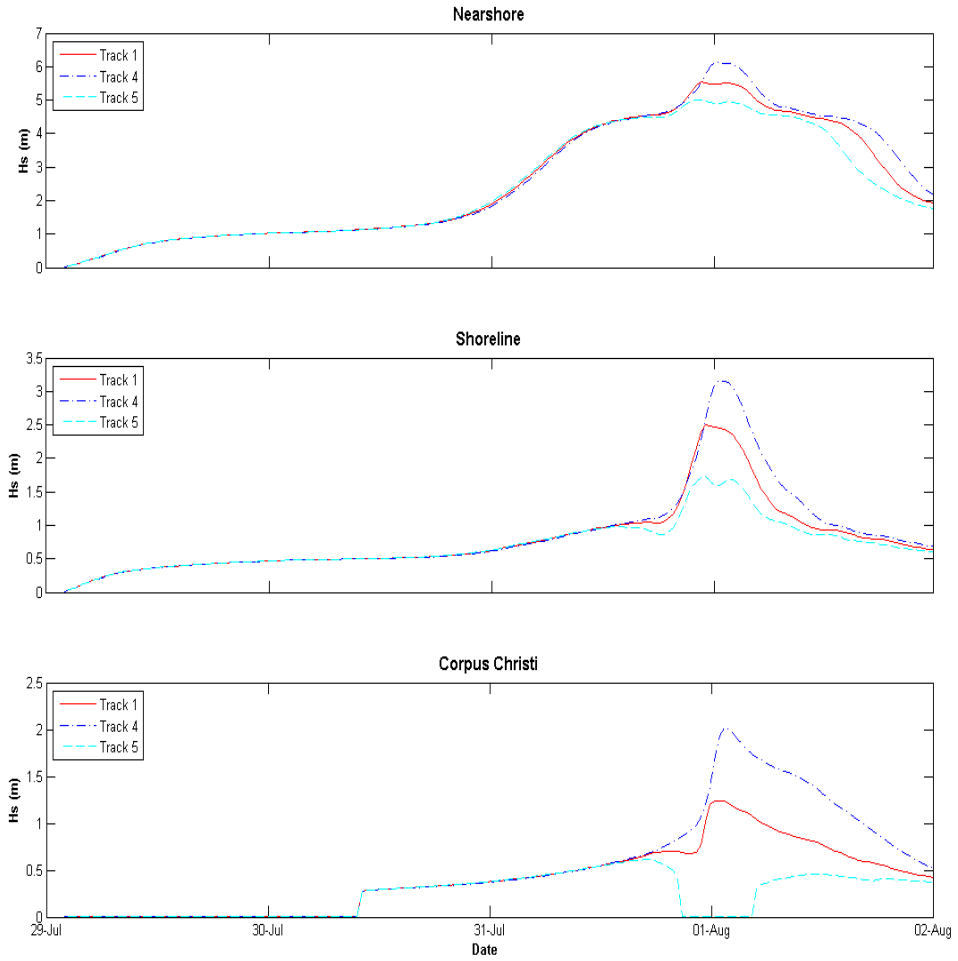

Figure 12. Time series of significant wave height (m) by track at near-shore (top), shoreline (middle) and Corpus Christi (bottom) locations as shown in Figure 9. All locations have different vertical plot ranges.

Inside the bay, near Corpus Christi, the extent of the maximum wave height for the storm on track 4, starts from the time of landfall until the end of simulation. The duration of the wave height is attributed to the wind velocity vectors directed across the bay at the period of landfall, which generates the maximum wave height. Furthermore,

due to the track of this storm, the outer most wind velocity vectors, after landfall, are directed northward across the bay; thus, occurring over a relatively long distance over which maximum waves can be generated. The time series of the wave height on track 5 produced the minimum wave height when compared to the other tracks. Inside the bay, at around the time of landfall, the wave height drops to zero and is then regenerated a few hours later. From the snapshots in Figure 11, the time period in which the wave height is zero corresponds to the weaker wind velocity vectors, on the left side of the storm, that are directed shoreward across the bay. This resulted in much lower surge elevations. The increase in wave height a few hours later resulted from the wind velocity vectors directed northwards across the bay, which subsequently elevated surge levels and generated waves.

4.3 Sensitivity to Hurricane Intensity

The sensitivity analyses compares the effects of varying the central pressures for three hurricanes approaching on track 1 from the southeast with a forward speed of 5.7m/s, radius of 20.4 km and making landfall at point 5 as indicated in Figure 9. Planar view elevation snapshots taken at different times in the simulation are displayed in Figure 13. These time frames show the wave heights at 6 hours before landfall, at landfall, and at 6 hours after landfall, and show the wave heights in relation to the hurricane as it approaches and passes over the bay. For each of the snapshots, the increase in central pressure of the storm translates into an increase in the magnitude of

the wind velocity vectors, which corresponds to the subsequent increase in wave heights and wave activity displayed in the various locations in the figure.

At 6 hours before landfall, the waves along the shoreline for the three storms are on the order of a meter. Also, during this time period, the wave heights offshore are increasing for the relative decrease in storm central pressure. At landfall, the winds shift northward and onshore; hence, the barrier islands immediately in front of the bay have been inundated with storm surge. Also, at this time inside the bay, the waves generated are due to a combination of localized hurricane winds and elevated water levels from the flooded barrier islands. After landfall and as each storm continue northwest the winds over the bay reverses direction. At 6 hours after landfall, with the winds directed northward, the largest wave height of around 7m is located in the offshore environment and corresponds to the storm with central pressure of 900mb. In the near-shore environment, water levels are returning to its pre-storm levels; hence, wave height is suppressed with model results of around 2m.

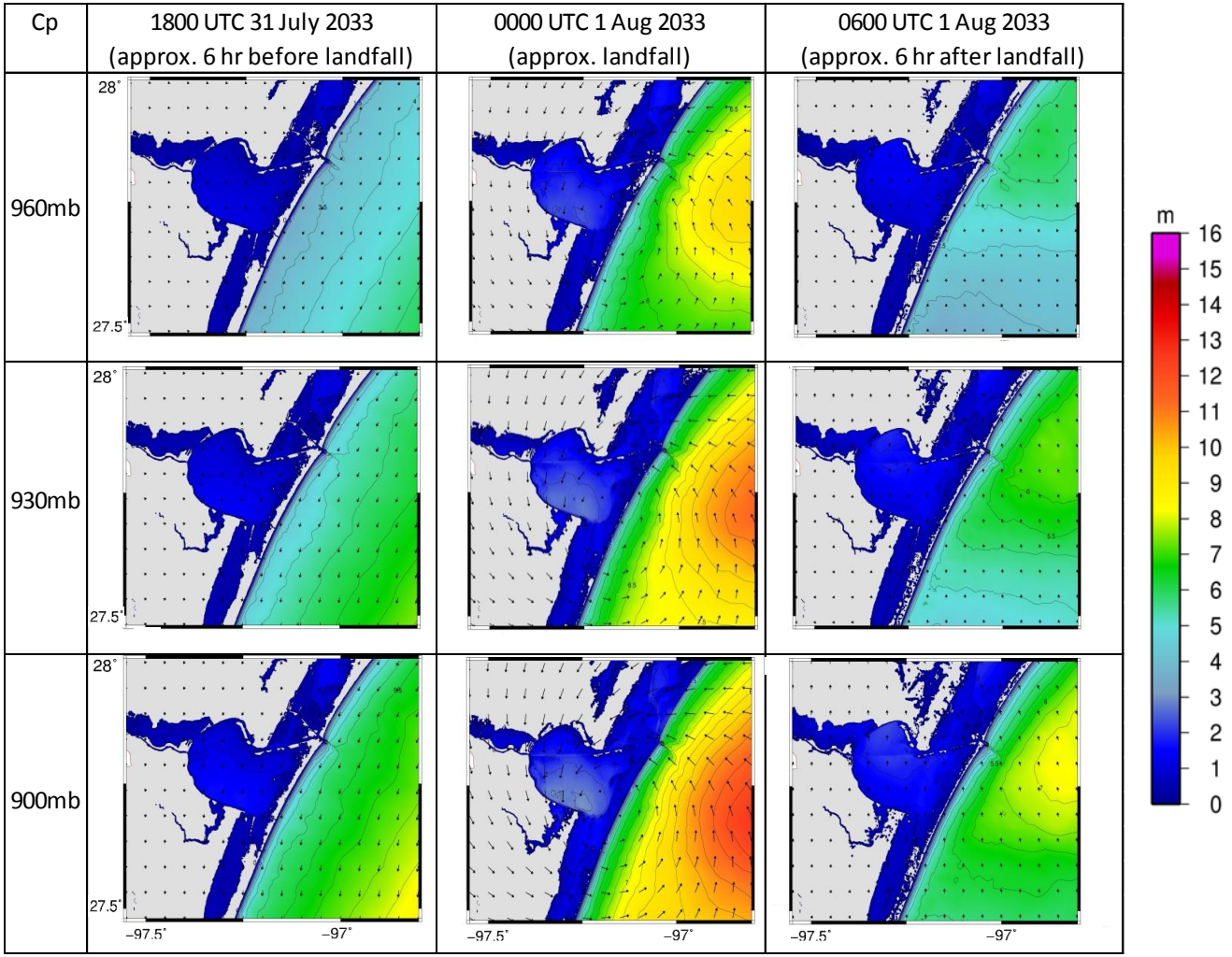

Figure 13. Results depicting sensitivity of wave heights to hurricane's central pressure simulated on track 1. Plots depicts planar view of model-simulated significant wave height contours (m) and wind vectors (m/s) snapshots at 6 hours before landfall, approximately landfall, and 6 hours after landfall. Rows represents the specified hurricane's pressure.

The spatial extent of the maximum wave heights generated for each storm, during the simulation, is showed in Figure 14. This figure illustrates that stronger hurricanes winds associated with the decrease in central pressure, generate higher waves. As shown in the figure, the strongest hurricane (900mb central pressure) generates a larger spatial extent of waves in the southern areas of the bay, at the shoreline, and in the near-shore environment.

Time series of the model-simulated wave heights at the near-shore, shoreline and Corpus Christi location are shown in Figure 15. At the specified points, the graphs display similar trends in terms of shape and temporal distribution of wave heights. In the near-shore environment, wave heights began increasing at around 24 hours before landfall, and subsequently start declining for a period of 24 hours after landfall. Within this window, for each storm the peak wave height is reached at around the time of landfall. At the shoreline, the situation is a bit similar; however the time window of increasing wave height is much narrower. Inside the bay, near Corpus Christi, there is a gradual increase in wave height until the hurricane makes landfall, though with zero wave height until the storm begins to affect the bay.

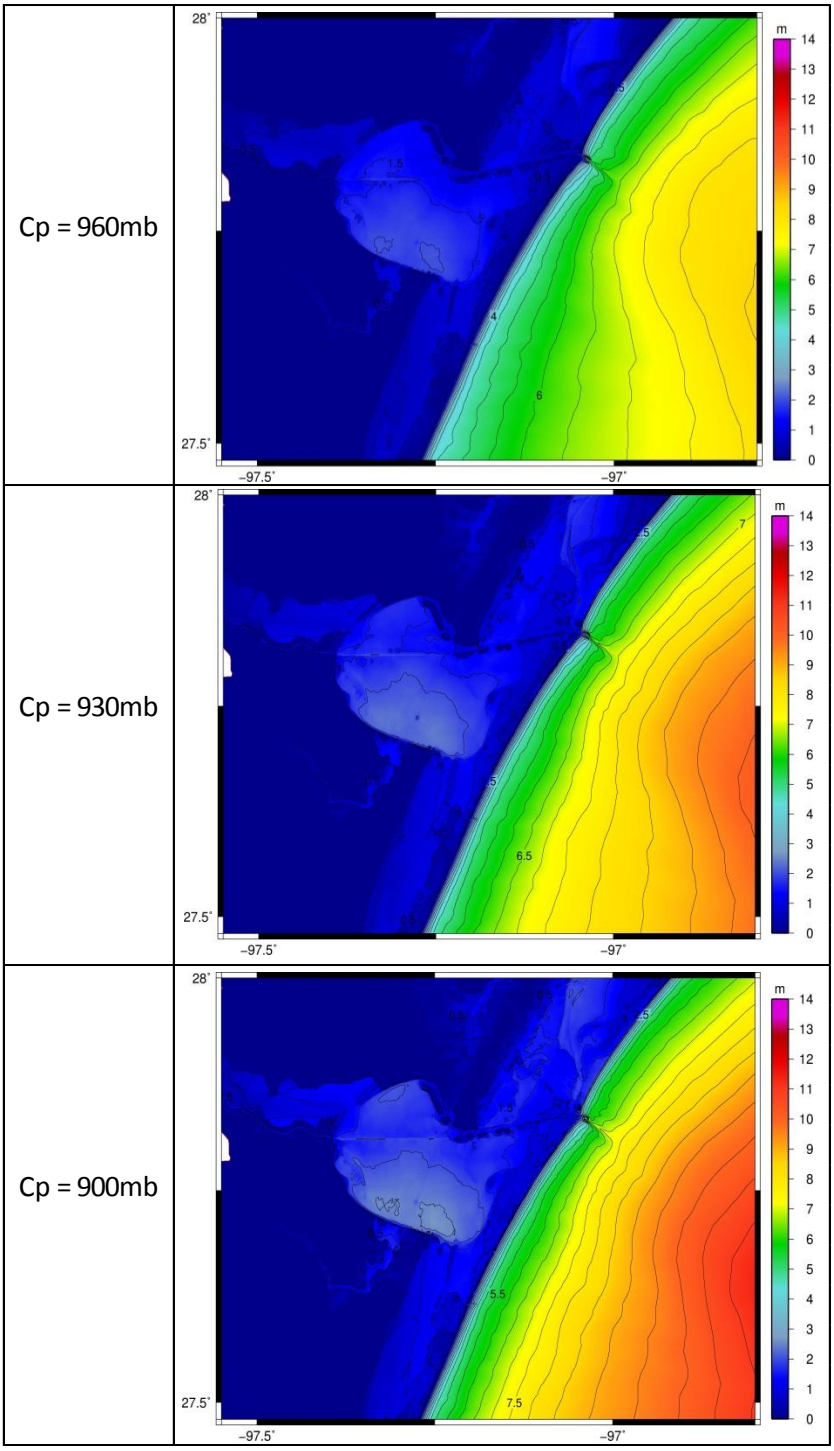

Figure 14. Results depicting spatial extent of contours of maximum significant wave height (m) during model simulation. Rows represent hurricane with central pressure of 960mb (top), 930mb (middle) and 900mb (bottom).

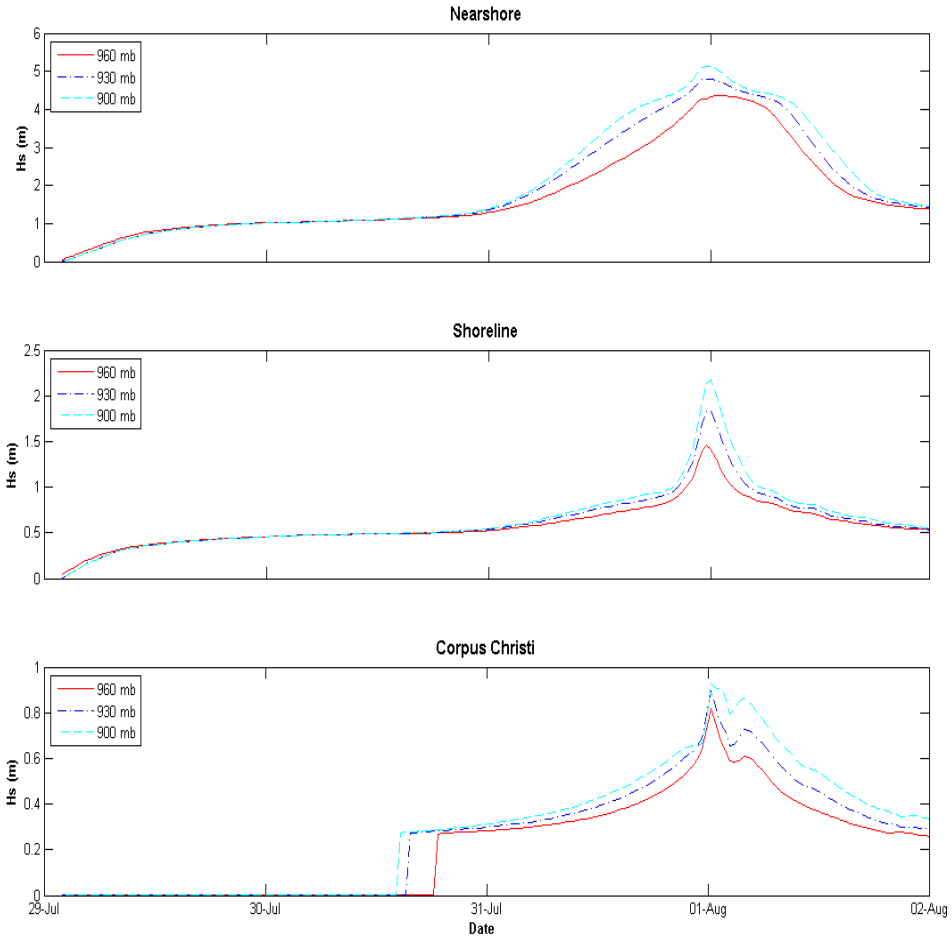

Figure 15. Time series of significant wave height (m) by hurricane's central pressure at near-shore (top), shoreline (middle) and Corpus Christi (bottom) locations. All locations have different vertical plot ranges.

4.4 Sensitivity to Hurricane Radius

This sensitivity analyses compares the effects of varying the radii for three hurricanes approaching from the southeast at 5 m/s, central pressure of 900mb, and making landfall at point 5 as indicated in Figure 9. Planar view elevation snapshots taken at different times in the simulation in displayed in Figure 16. These time frames show the wave heights at 6 hours before landfall, at landfall, and at 6 hours after landfall. The wave heights are shown in relation to the hurricane as it approaches and passes over the bay and shelf. For each of the snapshots, the increase of the storm radius produces an increase in the spatial distribution of intense wind velocity vectors, which corresponds to the subsequent increase in wave heights as displayed in the various locations on the figure.

At 6 hours before landfall, a southerly, alongshore-directed wind stress begins to affect the coast; however, the waves along the shoreline for the three storms are varying in magnitude and range between 2m – 3m. However, due to the spatial extent of the hurricane's outermost wind velocity vectors, the largest hurricane with a radius of 60m generates maximum wave heights of 10m in the offshore environment. For the same time period, the hurricane of radius 40m generates maximum wave heights of 8m, while the hurricane of radius 20m generates maximum wave heights of 6m. Additionally, at this time period, the outermost wind velocity vectors of the largest hurricane generate wave activity in the bay while the hurricane is still further offshore.

At landfall, in the near-shore environment, the hurricane with the largest radius continues to generate the largest maximum wave heights of around 10m; however, the

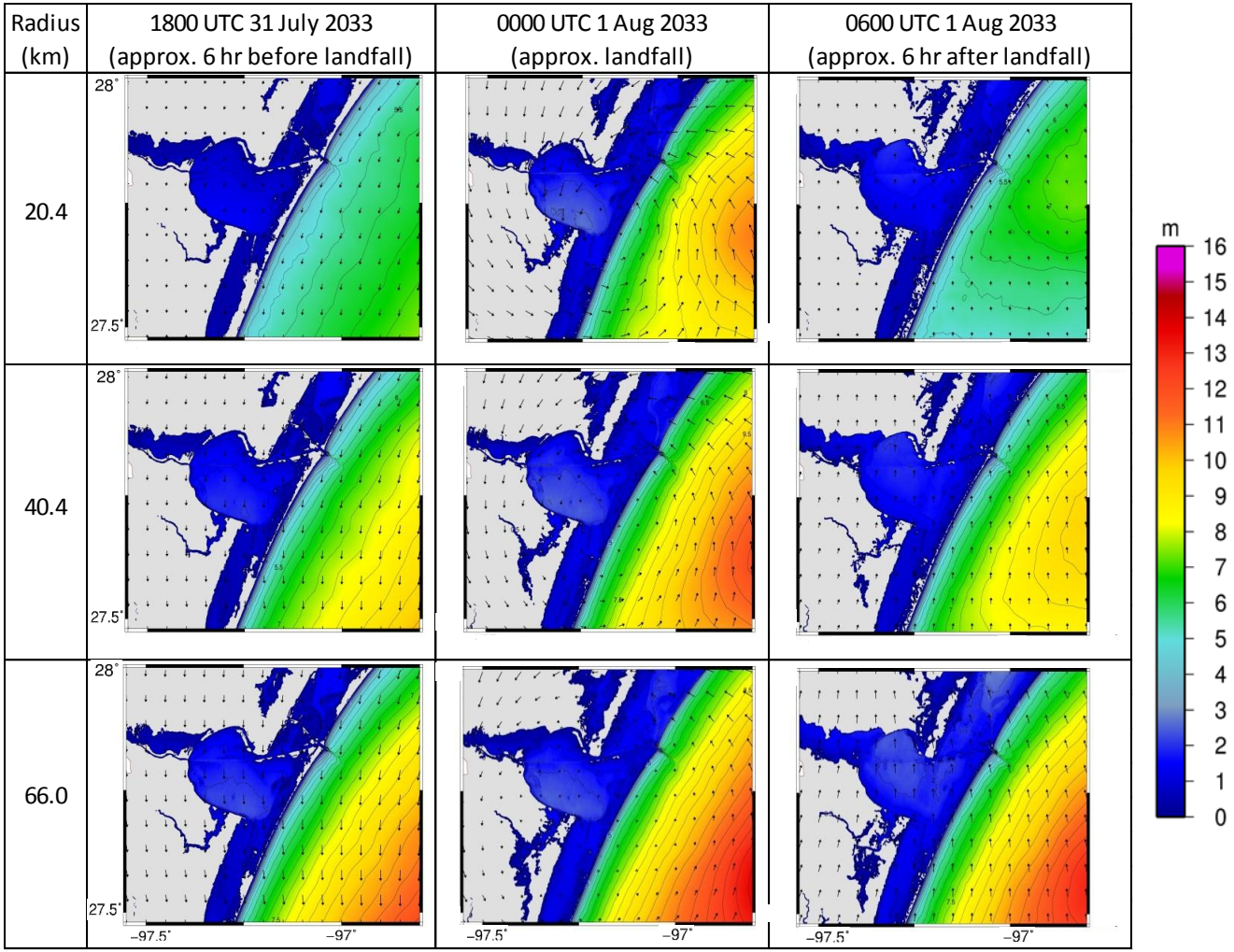

Figure 16. Results depicting sensitivity of wave heights to hurricane's radius on track 1. Plots depicts planar view of model-simulated significant wave height contours (m) and wind vectors (m/s) snapshots at 6 hours before landfall, approximately landfall, and 6 hours after landfall. Rows represents the specified hurricane's radius.

spatial extent of these maximum waves is increased. This spatial extent of maximum waves decreases with the corresponding decrease in hurricane size. Inside the bay, the wave heights are around 2m – 3m for each storm. After landfall, as the storms continue northwest, the winds over the bay reverses direction and the larger outermost wind velocity vectors continue to exhibit wave activity in the bay.

At 6 hours after landfall, with the winds directed northward, the largest wave height of around 2m exists in the northern extent of the bay and is generate by the largest hurricane. In the offshore environment, a similar wave height activity is represented, as the largest hurricane outer most winds generate significant wave heights of around 10m. The spatial extent of these maximum waves, in the offshore, is smaller in size when compared to the period in which the hurricane made landfall. Additionally, in the offshore environment, the hurricane of radius 40m generates wave heights of around 8m, while the hurricane of radius 20m generates wave heights of around 6m. For this time period, these wave heights occur over a smaller spatial area and correspond to the wind velocity vectors of the hurricane which, due to its size, generates much smaller wave heights.

The spatial extent of the maximum wave heights generated for each storm, during the simulation, is showed in Figure 17. This figure shows that as the hurricane radius increases, the spatial extent and maximum wave height subsequently increases. As shown in the figure, the largest hurricane (66.0 km radius) generates a significant amount of wave activity in the bay, near-shore and shoreline environment. Likewise,

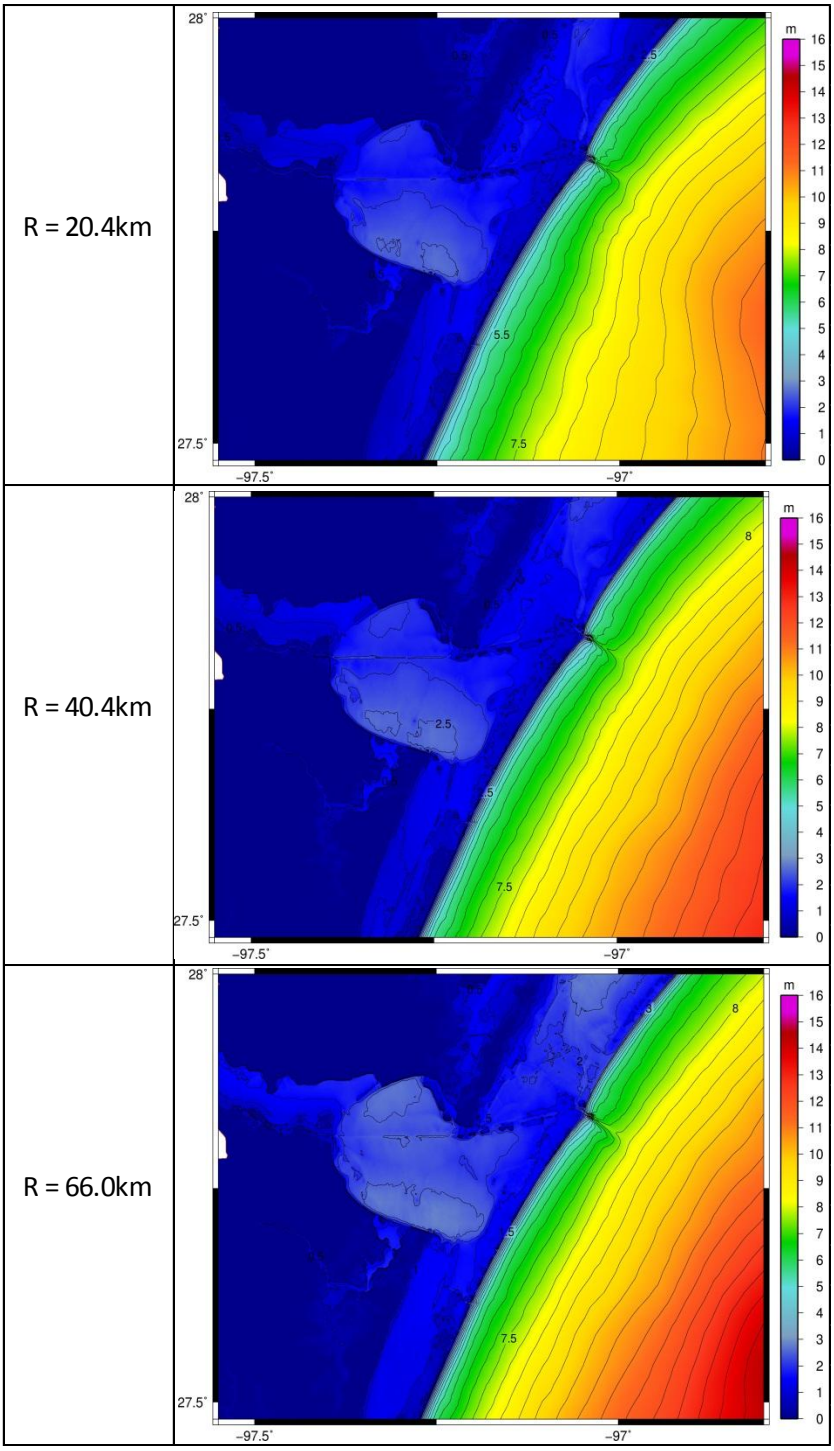

Figure 17. Results depicting spatial extent of maximum significant wave height contours (m) during model simulation. Rows represent hurricane with radius of 20.4km (top), 40.4km (middle) and 66.0km (bottom).

increasing maximum wave heights are shown offshore, for the corresponding increase in hurricane radius.

Time series of the model-simulated wave heights at the near-shore, shoreline and Corpus Christi locations are shown in Figure 18. For the points in the near-shore and at the shoreline, the time period of wave generation seems sensitive to the radius of the hurricane. In the near-shore environment, wave generation started rapidly more than 24 hours before the largest hurricane made landfall. This trend in the shape of the graph is similar for the smaller hurricanes; however the wave generation process is not as rapid and occurs over a smaller time period. Also, the temporal extent to which the waves remain near maximum height is much larger for the larger hurricanes as these waves remain in the intense region for a longer period of time. From the figure, it appears that the largest hurricane has two maxima that occur just before and after the hurricane made landfall. As the hurricane approach from the southeast the onshore directed winds produces a surge build up which enables maximum wave height in both the near-shore and shoreline locations. Also, shortly after the eye of the hurricane passes and the hurricane makes landfall, the offshore directed winds, under high surge conditions, enables maximum wave height in both the near-shore and shoreline locations.

After the hurricane made landfall, the decline in wave height over time is less steep for a larger hurricane than that of a smaller hurricane. Subsequently, higher wave heights remain much longer in the near-shore environment after the large hurricane has passed. This is evident from the planar plots (Figure 16) which depicts the maximum wave heights for the large hurricane remain in this environment 6 hours after it had made

landfall. Inside the bay, the wave generation process starts much earlier for larger hurricane than that of a smaller size. After maximum height is achieved, a similar gradual decline is observed for a larger hurricane than that of a smaller size hurricane.

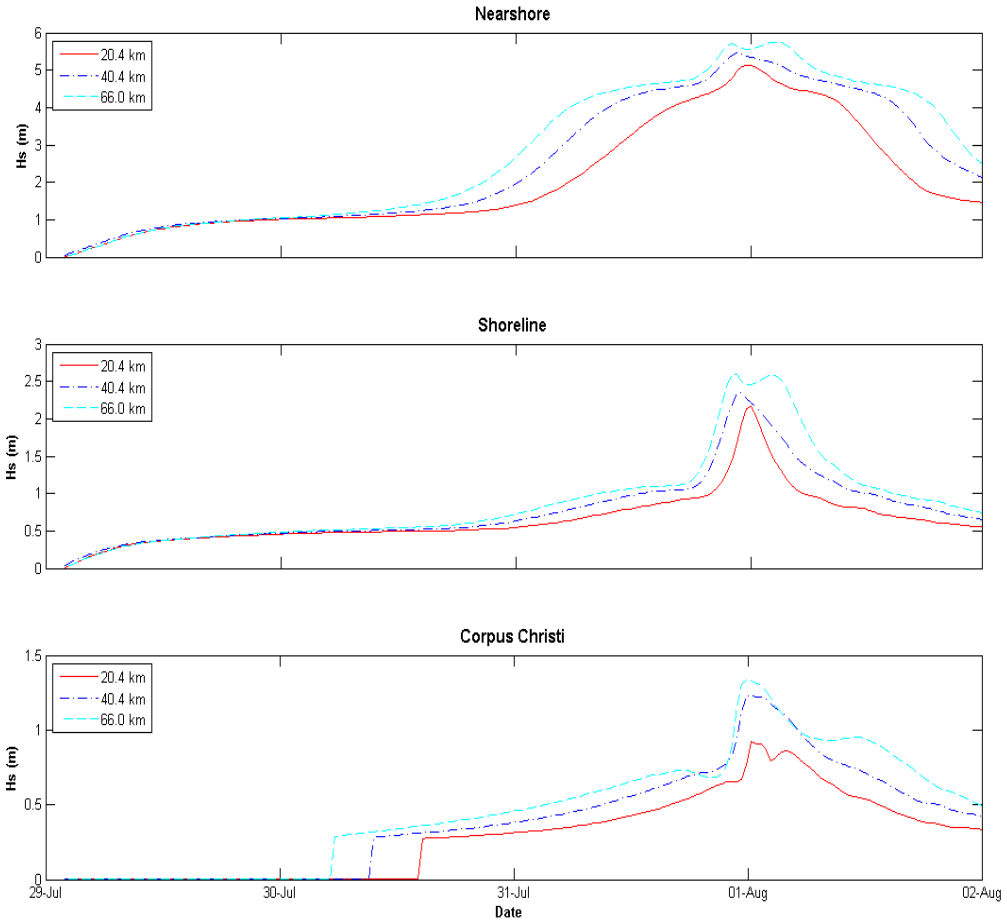

Figure 18. Time series of significant wave height (m) by hurricane's size at near-shore (top), shoreline (middle) and Corpus Christi (bottom) locations. All locations have different vertical plot ranges.

4.5 Sensitivity to Translational Speed

This sensitivity analysis compares the effects of varying the forward speed for the three hurricanes approaching from the southeast at 5 m/s, central pressure of 900mb, radius 38.9km and making landfall at point 5 as indicated in Figure 9. Because of the different forward speed of the hurricanes, the landfall times are also different, as displayed in the planar view elevation snapshots in Figure 19. These time frames show the wave heights at 6 hours before landfall, at landfall, and at 6 hours after landfall, and show the wave heights in relation to the hurricane as it approaches and passes over the bay. For each of the snapshots, the increase in forward speed of each hurricane generally corresponds into a smaller time period in which the hurricane winds can generate waves. Subsequently, for an increase in forward speed, there is a general decrease in wave heights as displayed in the various locations shown in the figure.

At 6 hours before landfall, the slower moving hurricane with 2.8 m/s forward speed displays significant wave activity in the offshore environment and inside the bay when compared to the hurricanes with 5.7m/s and 11.4 m/s forward speed. In this snapshot wave heights in the offshore environment are shown to be around 12m and the adjacent barrier islands appears to be flooded. Wave activity at the southern extent of the bay is due to the offshore directed wind velocity vectors. During this same time period, the faster moving hurricanes all display fewer flooded areas, smaller wave heights in the bay and in the near-shore environment.

At landfall, the intense winds to the right of the storm are directed onshore and there is an increase in over-land flooded areas for all hurricanes. For the hurricane

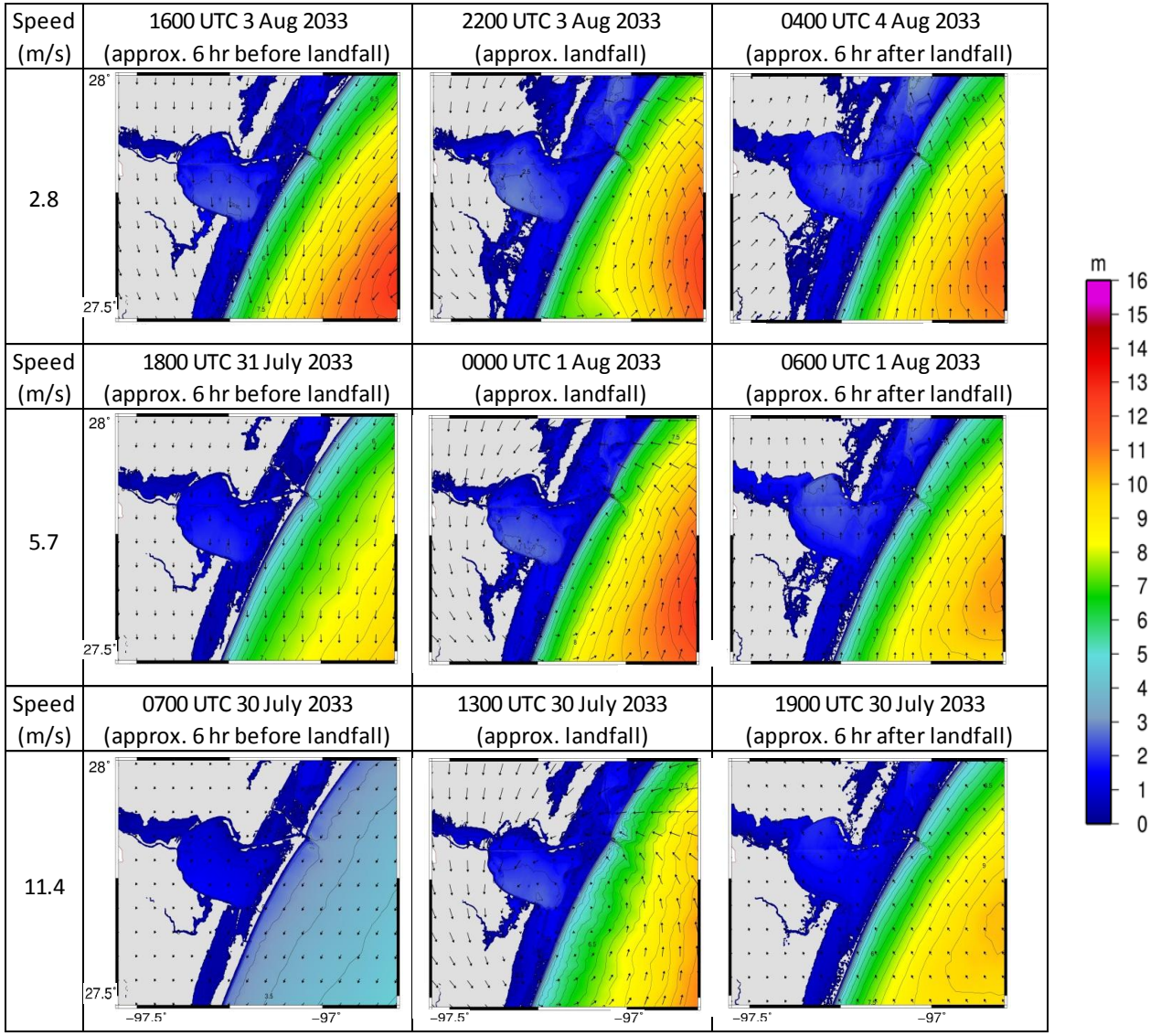

Figure 19. Results depicting sensitivity of wave heights to hurricane's forward speed. Plots depicts planar view of model-simulated significant wave height contours (m) and wind vectors (m/s) snapshots at 6 hours before landfall, approximately landfall, and 6 hours after landfall. Rows represents the specified hurricane's forward speed.

travelling at 2.8 m/s, the maximum wave heights of around 10m remain in the offshore environment; however, for the faster moving hurricanes there is an increase in wave activity in both the bay, near-shore and offshore environment. For the hurricane traveling at 5.7m/s near-shore wave heights are around 3m, while offshore maximum wave heights have increased to 10m. Similarly, for the hurricane traveling at 11.4m/s near-shore wave heights are around 3m, while offshore maximum wave heights has increased to 9m.

At 6 hours after landfall, with the winds directed northward, there are various levels of wave activity in the snapshot represented by the three hurricanes. For the hurricane travelling at 2.8 m/s, there still exist maximum wave heights of 10m in the offshore environments as these winds velocity vectors of this slow moving storm continue to generate these maximum wave conditions. Additionally, during this time period, wave heights of 3m are shown in the north-most location of Redfish Bay, due to the increase in water levels from the inundated barrier islands. In the offshore environment, the wind velocity vectors of the hurricane travelling at 5.7m/s generates maximum wave heights of around 9m, while the faster hurricane travelling at 11.4m/s generates maximum wave heights of around 8m. During this time period, all of the hurricanes show comparable wave heights of 2m – 3m in the near-shore environment.

The spatial extent of the maximum wave heights generated for each storm, during the simulation, is showed in Figure 20. This figure depicts that in the near-shore environment, the spatial extent of the wave height maxima is generally similar for all three hurricanes. This is not the case inside the bay as the hurricane travelling at 2.8 m/s

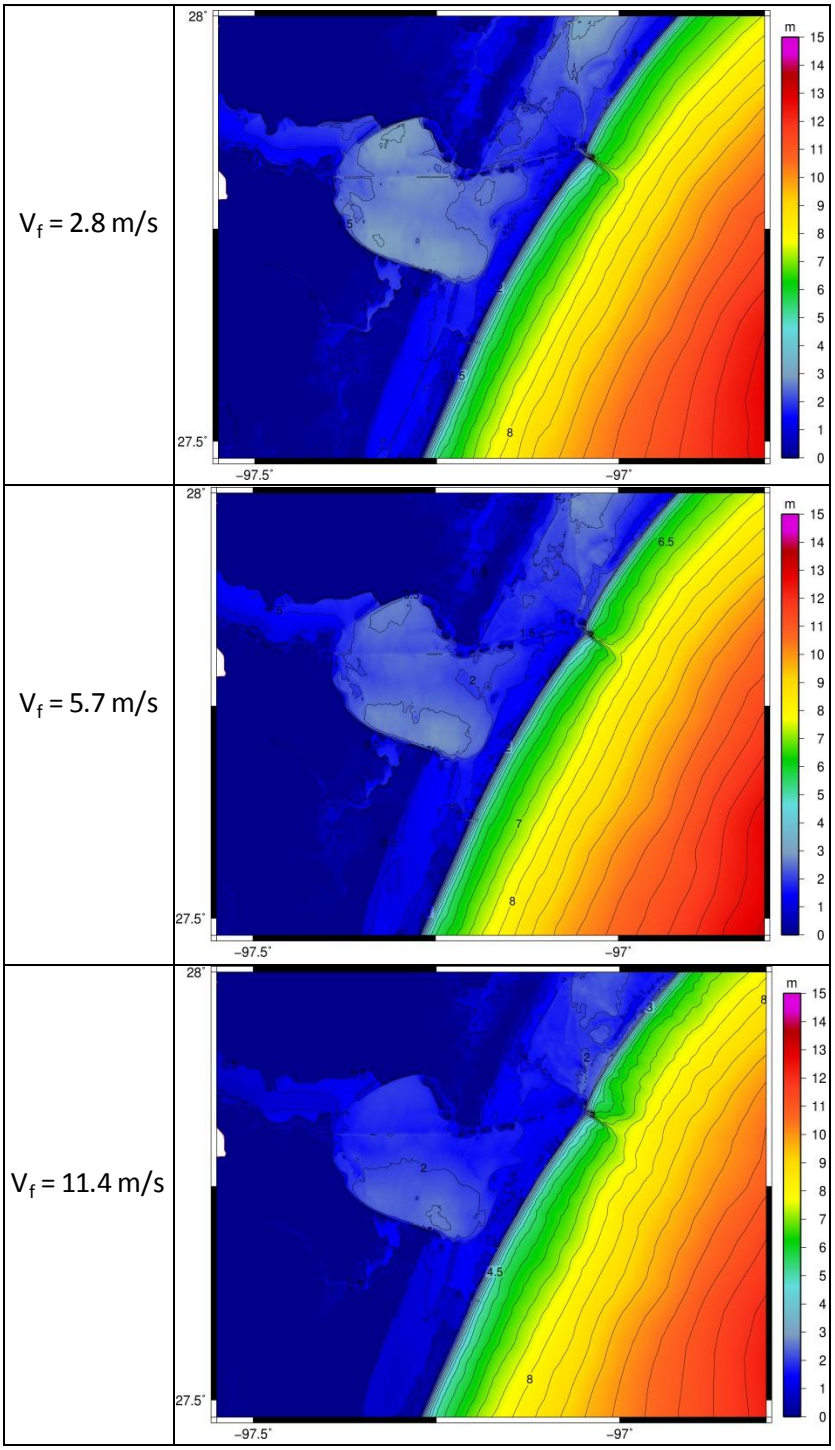

Figure 20. Results depicting spatial extent of maximum significant wave height contours (m) during model simulation. Rows represent hurricane with forward speed of 2.8m/s (top), 5.7m/s (middle) and 11.4m/s (bottom).

displays a significantly more spatial extent of maximum wave heights when compared to the hurricanes travelling at 5.7 m/s and 11.4 m/s, respectively.

Time series of the model-simulated wave heights at the near-shore, shoreline and Corpus Christi locations are shown in Figure 21. For the points in the near-shore and at the shoreline, the maximum wave height achieved seems less sensitive to the forward speed of the translating as the graphs depict similar maxima at these locations. However, for the point located in the bay, wave generation is sensitive to the forward speed of the hurricane as the slower moving hurricane travelling at 2.8 m/s achieved the greatest wave height than the faster moving hurricanes travelling at 5.7 m/s and 11.4 m/s, respectively.

Figure 21 illustrates that the time for which the wind acts on a given coastal ocean or bay environment is important in generating the maximum wave height. At the near-shore and shoreline locations on the Gulf, even though the translation speed may vary, the wave height responses are similar because the winds are acting over a sufficient time to raise sea level there, and subsequently allowing for maximum wave height. However, for the point located inside Corpus Christi Bay, the wave height responses are different for the variation in the translation speed of each hurricane. At around the time for each respective storm landfall, the leading winds of the storm raises sea level in the bay. The trailing winds then lowers sea level. If the trailing winds arrives before the leading winds can fully affect significant surge height than the resulting surge height will be suppressed. As a result, the slower the translation speed the larger the surge and wave height within the bay.

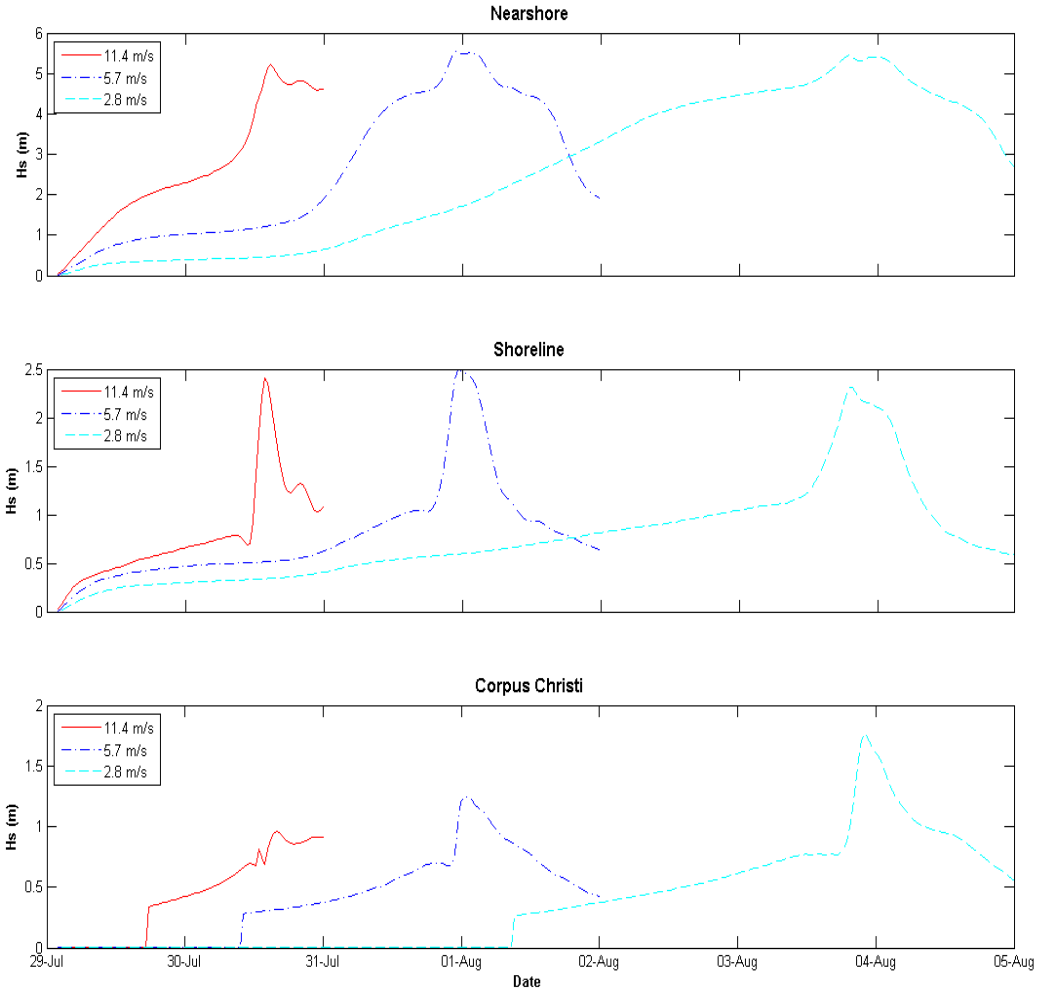

Figure 21. Time series of significant wave height (m) by hurricane's forward speed at near-shore (top), shoreline (middle) and Corpus Christi (bottom) locations. All locations have different vertical plot ranges.

4.6 Conclusions on Sensitivity Analysis

Presented in this section are the results of wave height sensitivity analysis based on the hurricane's landfall location, intensity, radius size and forward approach speed. Simulated planar elevation snapshot plots and time series graphs provide a spatial and temporal illustration of the characteristic impacts on significant wave heights.

The point of landfall is important because with counterclockwise winds around the hurricane eye, maximum surge and wave height levels are created by onshore-directed winds. This occurs when the landfall location is south of the Corpus Christi Bay. The central pressures and the physical size (radius to maximum winds) are also highly relevant. Intense storms consisting of low central pressure have maximum wind speeds that produces surge levels and maximum wave heights at locations located at the shoreline and in the bay. Similarly, storms with large radii have large winds extending over larger areas than smaller radii storms, thus producing a similar trend in wave height characteristics. Finally, the speed of approach is important since it takes a finite amount for time to transport water from one point to another in order to build the slope. Fast moving storms may yield lesser surge than slow moving storms since there may not be sufficient time to fully set up the sea surface slope that comprises the surge. As a result of lower surge levels, fast moving storms produces lower maximum wave height than slower moving storms.

One feature that is apparent is that each location (near-shore, shoreline and Corpus Christi) appears to have a time evolution trend that is unique to its location, regardless of the hurricane parameter being tested. The wave height at the near-shore

location builds up steadily, and the shape of its maximum is somewhat broad over time. The increase in water level due to surge might not be large here relative to depth, so the evolution is likely just due to the changes in wind speed alone. At the shoreline, there is a buildup of wave height that ramps up suddenly and also decays suddenly. Here the surge-induced increase in water level may be greater than the water depth, so breaking is keeping the wave height down until the surge gets high enough to allow the wave heights to grow – this is likely happening during the sudden increase near the landfall time. Finally, the Corpus Christi location appears to have a trend similar to the near-shore location, with the difference that the wave height is zero until the hurricane begins to affect the bay.

4.7 Development of Parameterized Models

Presented in this section are the results of the development of the parameterized maximum wave height response ($H_s^{\max}$) models. This is determined by incorporating Young's equivalent fetch (X_{eq-Y}) (Equation 2.16), Alves's modified version of Young's equivalent fetch (X_{eq-AY}) (Equation 2.19), and Alves's equivalent fetch (X_{eq-A}) (Equation 2.21) models into (1) dimensionless best-fit equations and (2) SPM model.

4.7.1 Dimensionless Functions Approach

For the points on the open coastline and at the near-shore location, Figure 22 illustrates the relationship between the dimensionless significant wave height and the three dimensionless forms of the equivalent fetch as discussed in Section 2.6. To obtain

a form similar to that of Young's maximum wave height prediction model (Equation 2.15), a power-based best-fit line was selected. Solving this equation for $H_s^{\max}$ yields formulas for predicting the maximum significant wave heights in the open-coast environment based on the gravitational constant (g), equivalent fetch (X_{eq}), and maximum wind speed (V_{max}). These formulas are represented as:

$$H_s^{\max} = 0.0002\left(\frac{V_{\max}^2}{g}\right)\left(\frac{gX_{eq-Y}}{V_{\max}^2}\right)^{0.51}, \tag{4.1}$$

$$H_s^{\max} = 0.0002\left(\frac{V_{\max}^2}{g}\right)\left(\frac{gX_{eq-AY}}{V_{\max}^2}\right)^{0.58}, \tag{4.2}$$

$$H_s^{\max} = 0.0022\left(\frac{V_{\max}^2}{g}\right)\left(\frac{gX_{eq-A}}{V_{\max}^2}\right)^{0.37}, \tag{4.3}$$

where Equations 4.1 – 4.3 represents the $H_s^{\max}$ formulas from the top to bottom graphs in Figure 22, respectively. Equations 4.1 and 4.2 each have similar coefficients and exponents because the functional form of X_{eq-Y} and X_{eq-AY} are both similar. This is in contrast to Equation 4.3 which incorporates X_{eq-A} , whose functional form is significantly different as it includes both R_{max} (and not Young's scaling relationship) and $c_g^{\max}$.

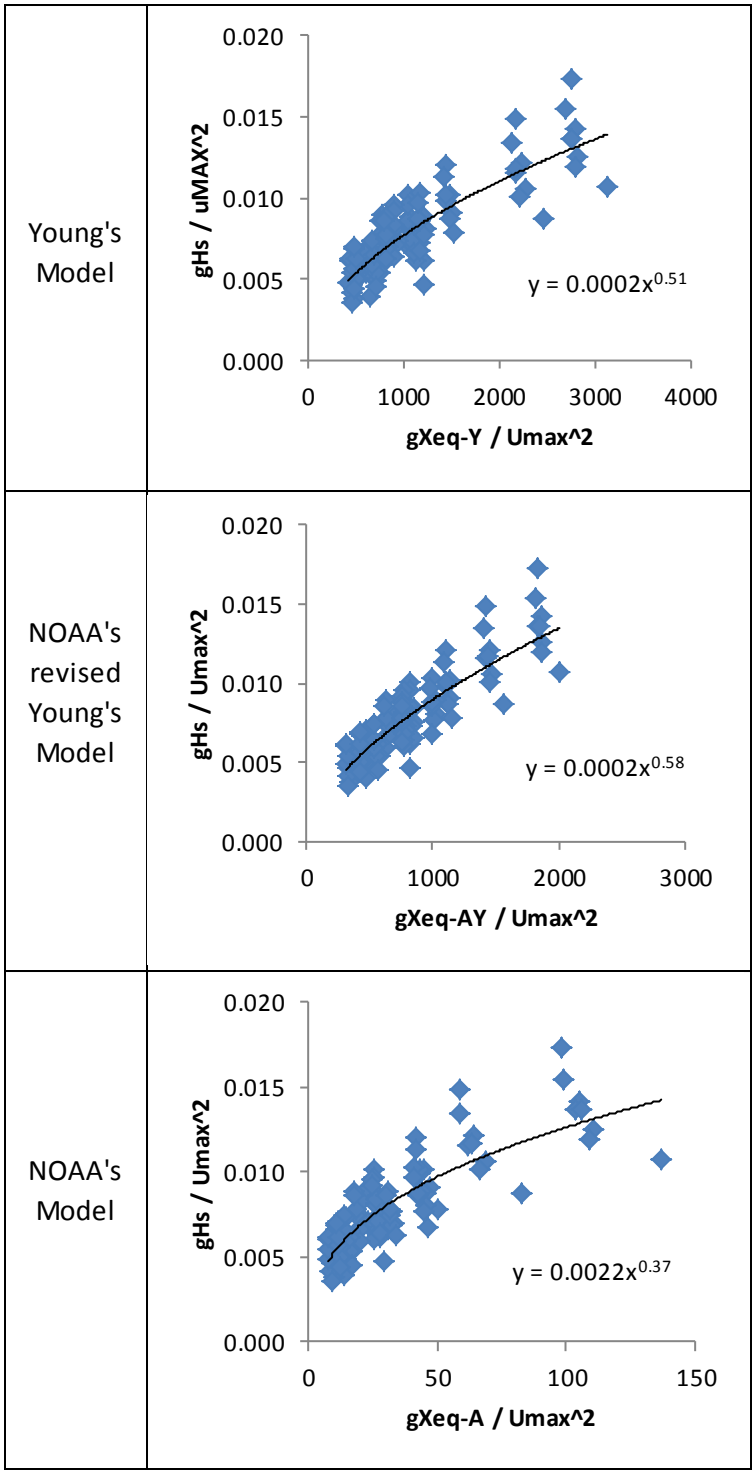

Figure 22. Dimensionless relationships for the points located at the shoreline. Modeled data shown as scatter points with the associated power based best-fit curves. Rows represents the use of Xeq as defined by Young (top), Alves-Young (middle), and Alves (bottom).

For the points that are stationed inside the bay, Figure 23 illustrates the relationship between the dimensionless significant wave height and the three forms of the equivalent fetch as previously mentioned. Solving the power-based best-fit line for $H_s^{\max}$ yields formulas for predicting the maximum significant wave height inside the bay, which are represented as:

$$H_s^{\max} = 0.0002\left(\frac{V_{\max}^2}{g}\right)\left(\frac{gX_{eq-Y}}{V_{\max}^2}\right)^{0.47}, \tag{4.4}$$

$$H_s^{\max} = 0.0001\left(\frac{V_{\max}^2}{g}\right)\left(\frac{gX_{eq-AY}}{V_{\max}^2}\right)^{0.57}, \tag{4.5}$$

$$H_s^{\max} = 0.0024\left(\frac{V_{\max}^2}{g}\right)\left(\frac{gX_{eq-A}}{V_{\max}^2}\right)^{0.29}, \tag{4.6}$$

where Equations 4.4 – 4.6 represents the $H_s^{\max}$ formulas from the top to bottom graphs in Figure 23, respectively.

An evaluation of the accuracy of Equations 4.4 – 4.6 is presented in Figure 24, as the $H_s^{\max}$ predicted, for all 24 points, through these equations are compared with the $H_s^{\max}$ output from the ADCIRC-SWAN simulations. The top graph in this figure displays the $H_s^{\max}$ predicted using Equations 4.1 and 4.4, using X_{eq-Y}, has a R^2 value of 0.37 and root mean square error of 0.56 m. The middle graph in this figure displays the $H_s^{\max}$ predicted using Equations 4.2 and 4.5, using X_{eq-AY}, has a R^2 value of 0.28 and root mean square error of 0.68 m. The bottom graph in this figure displays the $H_s^{\max}$

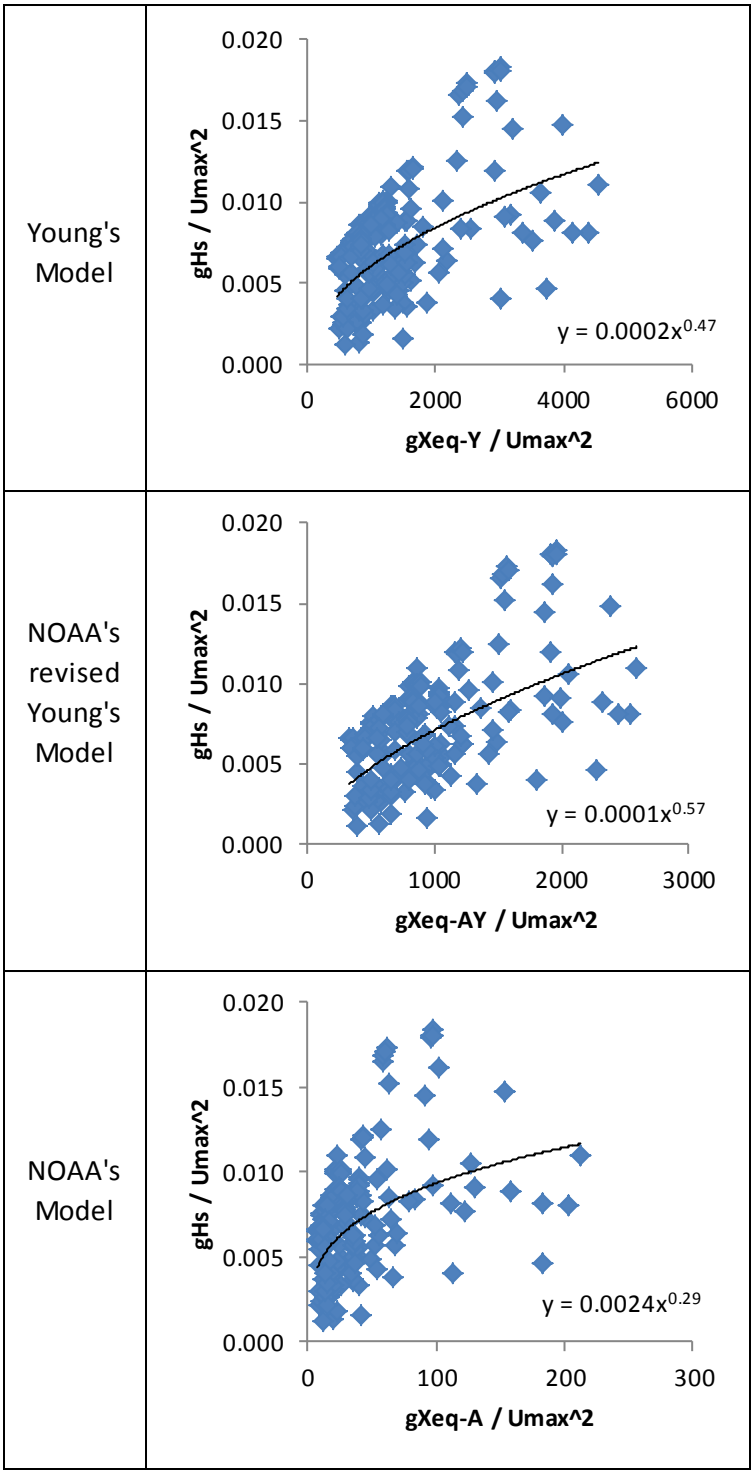

Figure 23. Dimensionless relationships for the points located in the bay. Modeled data are shown as scatter points with the associated power based best-fit curves. Rows represents the use of Xeq as defined by Young (top), Alves-Young (middle), and Alves (bottom).

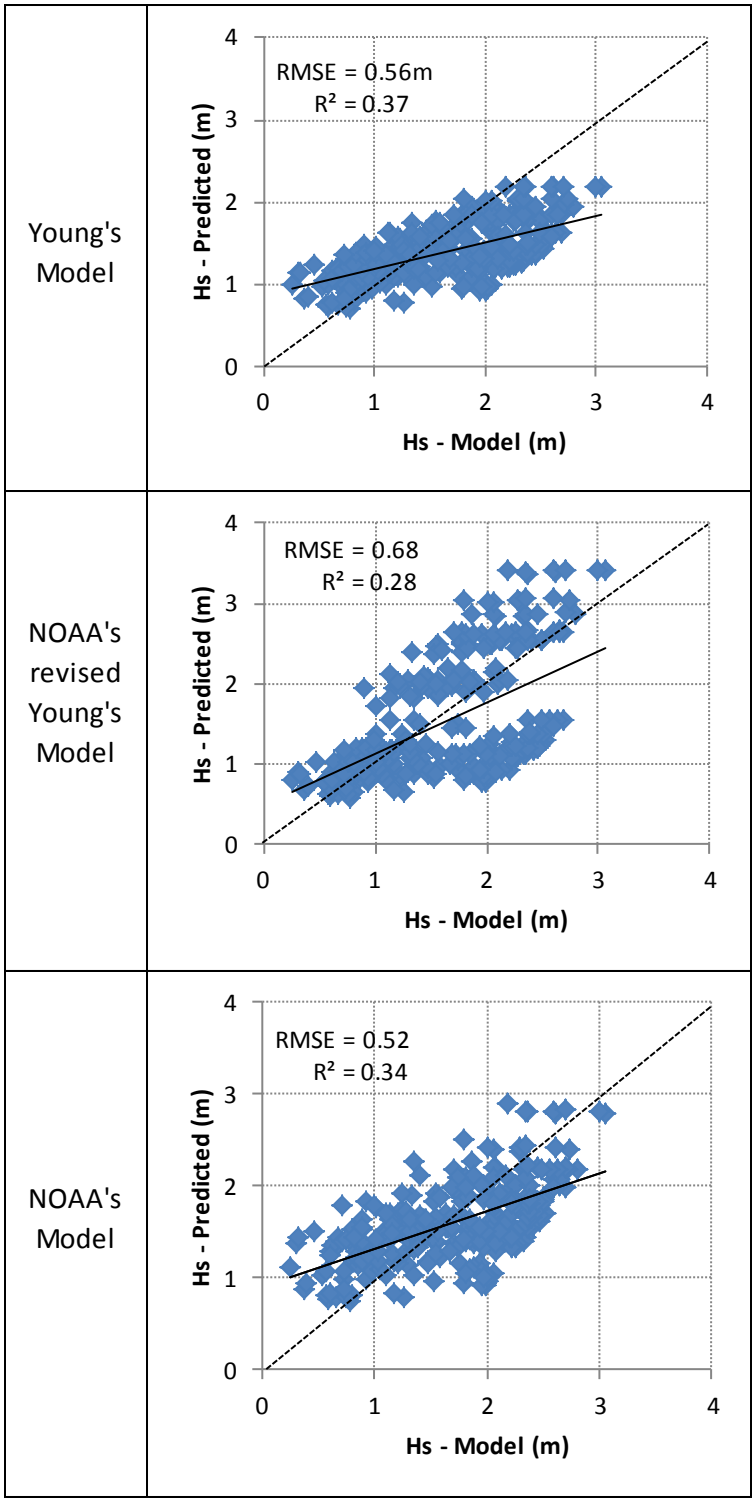

Figure 24. Scatterplots of predicted maximum significant wave height determined from dimensionless functions compared with numerical model results. Rows represents the max wave height based on Eqns. 4.1 and 4.4 (top), Eqns. 4.2 and 4.5 (middle), Eqns. 4.3 and 4.6 (bottom).

predicted using Equations 4.3 and 4.6, using X_{eq-A}, has a R^2 value of 0.34 and root mean square error of 0.52 m.

Table 6 displays a summary of the statistical analysis of $H_s^{\max}$ prediction error for the points on the open coast line and in the near-shore. For these points, X_{eq-A} model had slightly under-predicted $H_s^{\max}$, with an average bias of -0.07m. This is significantly less than X_{eq-Y} with a bias of -0.22m. However, X_{eq-AY} had over-predicted $H_s^{\max}$ with an average bias of 0.41m. Also, X_{eq-A} model has an equal scatter index to that of X_{eq-Y}, with an average value of 0.28. Hence, these methods have a better accuracy of $H_s^{\max}$ than that of X_{eq-AY}, which had a scatter index value of 0.41.

At the shoreline, the variation in the individual biases at the points 2 -10, gives an indication of how strongly the various forms of the equivalent fetch and the bathymetric depth ultimately determines the predicted $H_s^{\max}$, from the dimensionless functions. This is evident as X_{eq-Y} and X_{eq-AY} have a similar structure and differ slightly in terms of coefficients and exponents, yet they display a wide range of biases for the respective points. For instance point 2, located west of the hurricane landfall at a depth of 0.13m, had an average bias of 0.04m for X_{eq-Y}, 0.74m for X_{eq-AY}, and 0.22m for X_{eq-A}. Similarly, point 6 located on the dune at an elevation of -0.75m had an average bias of 0.26m for X_{eq-Y}, 0.96m for X_{eq-AY}, and 0.48m for X_{eq-A}.

Table 7 displays a summary of the statistical analysis of $H_s^{\max}$ prediction error for the points in the bay. For these points, X_{eq-A} model had the least under-prediction of

Table 6. Summary of average errors, for the dimensionless functions, at the points located on the open-coast line.

	Open Coast Maximum Wave Heights - (Dimensionless functions)					
	Young's Model		NOAA-Young's Model		NOAA's Model	
Point	SI	Bias (m)	SI	Bias (m)	SI	Bias (m)
2	0.11	0.04	0.44	0.74	0.16	0.22
3	0.13	-0.20	0.27	0.50	0.07	-0.04
4	0.08	0.04	0.44	0.74	0.15	0.22
5	0.13	-0.21	0.27	0.52	0.07	-0.04
6	0.21	0.26	0.66	0.96	0.34	0.48
7	1.22	-0.43	1.22	-0.43	1.22	-0.43
8	0.28	-0.65	0.07	0.07	0.22	-0.51
9	0.17	-0.30	0.22	0.42	0.09	-0.13
10	0.25	-0.57	0.09	0.16	0.19	-0.43
Average	**0.28**	**-0.22**	**0.41**	**0.41**	**0.28**	**-0.07**

Table 7. Summary of average errors, for the dimensionless functions, at the points located in the bay.

	Bay Maximum Wave Heights - (Dimensionless functions)					
	Young's Model		NOAA-Young's Model		NOAA's Model	
Point	SI	Bias (m)	SI	Bias (m)	SI	Bias (m)
11	0.44	-1.01	0.52	-1.18	0.36	-0.80
12	0.44	-0.98	0.51	-1.15	0.35	-0.78
13	0.37	-0.76	0.46	-0.93	0.28	-0.54
14	0.43	-0.97	0.51	-1.14	0.36	-0.78
15	0.41	-0.89	0.49	-1.06	0.33	-0.70
16	0.49	0.39	0.29	0.22	1.02	-0.85
17	0.28	0.24	0.14	0.07	0.56	0.51
18	0.94	0.57	0.66	0.39	1.33	0.82
19	0.36	0.27	0.19	0.10	0.56	0.47
20	0.19	-0.06	0.25	-0.23	0.16	0.07
21	0.29	-0.39	0.38	-0.56	0.21	-0.27
22	0.32	-0.54	0.41	-0.71	0.23	-0.40
23	0.29	0.21	0.15	0.04	0.46	0.40
24	0.15	0.06	0.15	-0.11	0.25	0.24
Average	**0.39**	**-0.27**	**0.37**	**-0.45**	**0.46**	**-0.19**

the $H_s^{\max}$ with an average bias of -0.19m. Also, both X_{eq-Y} and X_{eq-AY} had under-predicted $H_s^{\max}$ with an average bias of -0.27m and -0.45m, respectively. However, in terms of accuracy, X_{eq-AY} has a slightly higher scatter index average value of 0.37. This is followed by both X_{eq-Y}, with an average value of 0.39, and X_{eq-A}, with an average value of 0.46.

The grouping in the individual biases in the bay, at points 11 – 24, gives an indication of how strongly the geographical location of the points helps to determine the predicted $H_s^{\max}$, from the dimensionless functions. For points 11-15, which are located at the southern portion of the bay, each form of the X_{eq} all under-predicted the $H_s^{\max}$ by the various negative biases as indicated in the table. This could have resulted from the buildup of surge and flooding of this geographic location as the hurricane made landfall, thus enabling maximum wave conditions in this area. Ultimately, the relative large negative biases indicate that the models did not reflect this large increase in water level that would enable maximum wave heights. A similar scenario is indicated by points 20 – 22, which are located at the northern extent of the bay and displays relative lower negative biases. The geographic location of these points indicated that the surge build up cause by the weaker trailing wind velocity vectors, after the hurricane passes, also enable wave conditions that were slightly higher than the predicted $H_s^{\max}$ values. For points 16 – 19 , which are over-land and located in the western portion of the bay, the over-prediction of the models indicted that there was not a significant level of surge buildup at these points thus yielding lower wave activity. Similarly for points 23 – 24, which are

located in the adjacent Nueces Bay, the over-prediction of the models indicted that there was not a significant level of surge buildup at these points as the narrow inlet of this bay might have provided a restriction for surge development. This restriction in surge production would yield low wave activity.

4.7.2 SPM Model

The accuracy of the SPM model (Equation 2.28), for all output points, is presented in Figure 25, as the $H_s^{\max}$ predicted from this model (with the inclusion of X_{eq}) are compared with the $H_s^{\max}$ output from the ADCIRC-SWAN simulations. The top graph in this figure displays the $H_s^{\max}$, predicted using X_{eq-Y} with a R^2 value of 0.77 and root mean square error of 0.45 m. The middle graph in this figure displays the $H_s^{\max}$, predicted using X_{eq-AY} with a R^2 value of 0.77 and root mean square error of 0.45 m. The bottom graph in this figure displays the $H_s^{\max}$, predicted using X_{eq-A} with a R^2 value of 0.46 and root mean square error of 0.86 m.

To decrease the root mean square error in the SPM model, output points 1, located in the near-shore, and 16, located in the bay, are removed from the analysis. The removal of these points resulted in a 17.7% reduction of the root mean square error for the $H_s^{\max}$ predicted using X_{eq-Y} and X_{eq-AY}. Likewise, there is a 39.5% reduction in the root mean square error for the $H_s^{\max}$ predicted using X_{eq-A}. This reduction is presented in Figure 26 as the $H_s^{\max}$ predicted from this model are compared with the $H_s^{\max}$ output

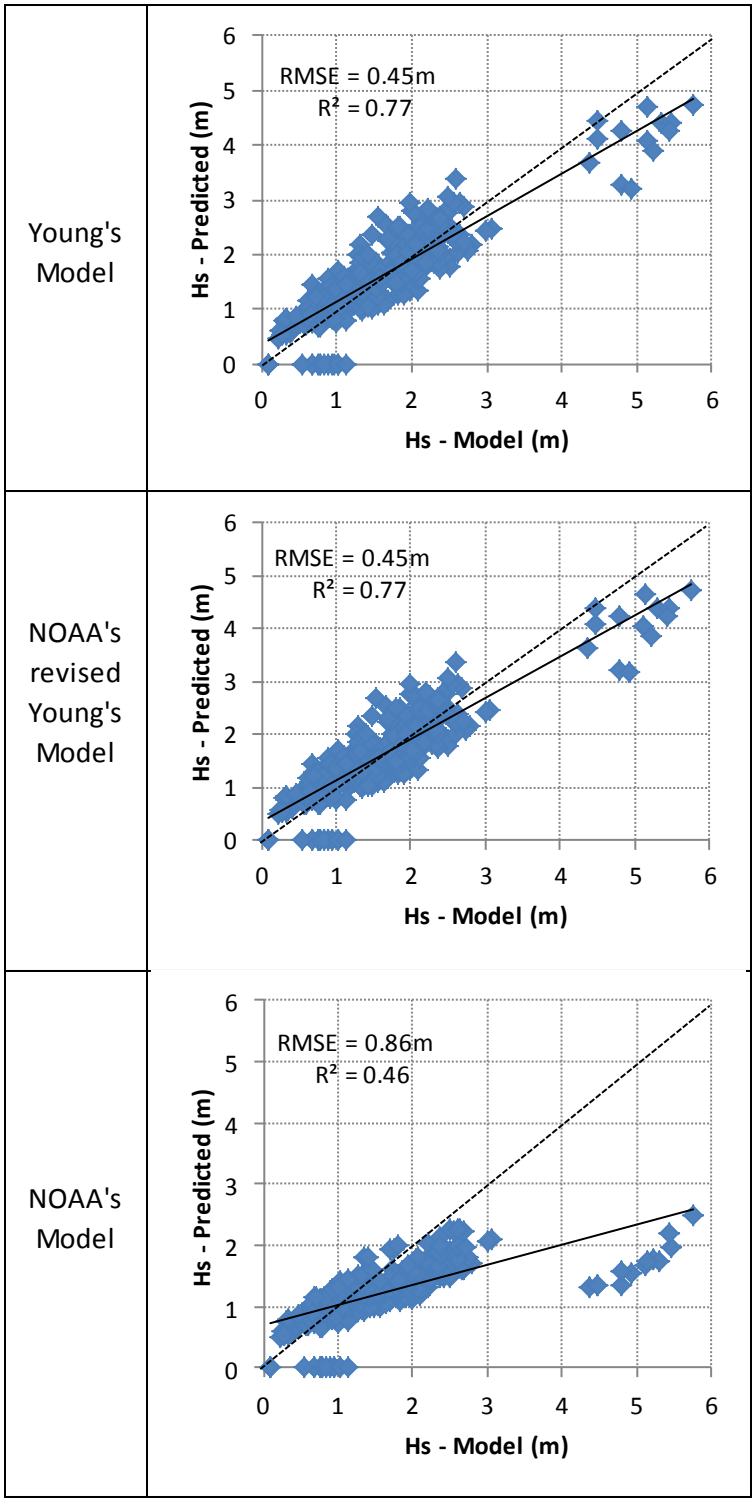

Figure 25. Scatterplots of predicted maximum significant wave height determined from the SPM model functions compared with numerical model results. Rows represents the use of Xeq, in the SPM model, as defined by Young (top), Alves-Young (middle), and Alves (bottom).

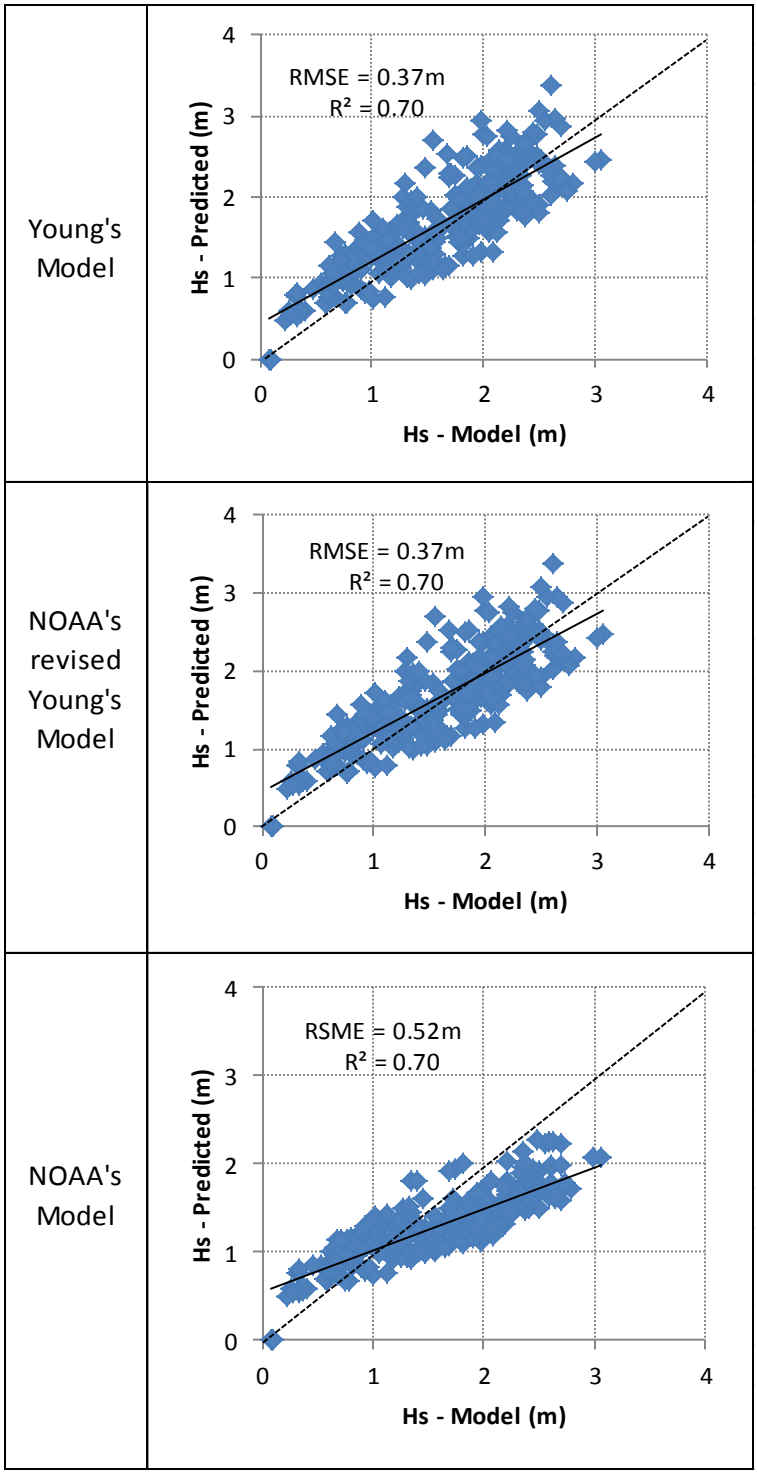

Figure 26. Scatterplots of predicted maximum significant wave height (minus points 1 and 16) determined from the SPM model functions compared with numerical model results. Rows represents the use of Xeq, in the SPM model, as defined by Young (top), Alves-Young (middle), and Alves (bottom).

from the ADCIRC-SWAN simulations. The top graph in this figure displays the $H_s^{\max}$, predicted using X_{eq-Y} with a R^2 value of 0.70 and root mean square error of 0.37 m. The middle graph in this figure displays the $H_s^{\max}$, predicted using X_{eq-AY} with a R^2 value of 0.70 and root mean square error of 0.37 m. The bottom graph in this figure displays the $H_s^{\max}$, predicted using X_{eq-A} with a R^2 value of 0.70 and root mean square error of 0.52m.

Table 8 displays a summary of the statistical analysis of $H_s^{\max}$ prediction error for the points on the open coast line. For these points, both X_{eq-Y} and X_{eq-AY} had under-predicted $H_s^{\max}$ with the same average bias value of -0.25m. This is significantly less than X_{eq-A} model which also under-predicted the $H_s^{\max}$, but with a higher a bias of -0.49m. Also, both X_{eq-Y} and X_{eq-AY} had a similar scatter index value 0.23. Hence, for the points located on the open coast, these methods have a better accuracy of $H_s^{\max}$ than that of X_{eq-A}, which had a higher scatter index value of 0.33.

At the shoreline, for points 2 – 10, the equal biases X_{eq-Y} and X_{eq-AY} as compared to the biases of X_{eq-A} 2 -10, gives an indication of how strongly the functional form of the equivalent fetch, when incorporated into the SPM model, determines the $H_s^{\max}$. This is in stark contrast to the variations in the biases produced from the dimensionless functions discussed in the previous section. Additionally, the SPM model

under predicted $H_s^{\max}$ for all the points at the shoreline, with the exception of the point 7, which is located inland.

Table 8. Summary of average errors, for the SPM model, at the points located on the open-coast line.

	Open Coast Maximum Wave Heights - (SPM)					
	Young's Model		NOAA-Young's Model		NOAA's Model	
Point	SI	Bias (m)	SI	Bias (m)	SI	Bias (m)
2	0.18	-0.26	0.18	-0.26	0.26	-0.42
3	0.18	-0.32	0.18	-0.32	0.30	-0.57
4	0.14	-0.19	0.14	-0.19	0.23	-0.38
5	0.16	-0.25	0.16	-0.25	0.29	-0.55
6	0.16	-0.17	0.16	-0.17	0.21	-0.28
7	0.62	0.21	0.62	0.21	0.60	0.20
8	0.22	-0.48	0.22	-0.48	0.38	-0.92
9	0.19	-0.34	0.19	-0.34	0.32	-0.65
10	0.20	-0.42	0.20	-0.42	0.37	-0.85
Average	**0.23**	**-0.25**	**0.23**	**-0.25**	**0.33**	**-0.49**

Table 9 displays a summary of the statistical analysis of $H_s^{\max}$ prediction error for the points in the bay. Unlike the open-coast points, both X_{eq-Y} and X_{eq-AY} had over-predicted the $H_s^{\max}$ with the same average bias value of 0.18m. On the other hand, X_{eq-A} model had under-predicted the $H_s^{\max}$ with an average bias of -0.25m. However, in terms of accuracy, all three methods produced similar scatter index average values. X_{eq-A}, just has a slightly more accurate value of 0.31, while both X_{eq-Y} and X_{eq-AY} had a similar scatter index value 0.33.

Table 9. Summary of average errors, for the SPM model, at the points located in the bay.

	Bay Maximum Wave Heights - (SPM)					
	Young's Model		NOAA-Young's Model		NOAA's Model	
Point	SI	Bias (m)	SI	Bias (m)	SI	Bias (m)
11	0.10	0.03	0.10	0.03	0.33	-0.74
12	0.11	0.12	0.11	0.12	0.32	-0.70
13	0.10	0.02	0.10	0.02	0.27	-0.54
14	0.09	0.08	0.09	0.08	0.32	-0.70
15	0.15	0.23	0.15	0.23	0.29	-0.60
16	1.02	-0.85	1.02	-0.85	1.02	-0.85
17	0.26	0.17	0.26	0.17	0.19	0.09
18	0.65	0.40	0.65	0.40	0.56	0.35
19	0.52	0.43	0.52	0.43	0.32	0.26
20	0.20	0.15	0.20	0.15	0.11	-0.04
21	0.23	0.26	0.23	0.26	0.15	-0.21
22	0.43	0.74	0.43	0.74	0.16	-0.25
23	0.41	0.36	0.41	0.36	0.23	0.21
24	0.40	0.42	0.40	0.42	0.15	0.16
Average	**0.33**	**0.18**	**0.33**	**0.18**	**0.31**	**-0.25**

For points 11 – 24 in the bay, the equal over-prediction by both X_{eq-Y} and X_{eq-AY} in the SPM gives an indication of how strongly the functional form of the equivalent fetch, when incorporated into the SPM model, determines the $H_s^{\max}$. The range of over-prediction, for X_{eq-Y} and X_{eq-AY}, across all the points seem to indicate that geographical location does not play an influence and the wave growth as govern by SPM seem to work well in the bay. The biases produced by these forms of X_{eq} are different than the grouping of the individual biases given by X_{eq-A} for the points in the bay. The grouping observed, for this form of the equivalent fetch, is an indication of how

the geographical location of points 11 – 24, helps to determine the predicted $H_s^{\max}$. The grouping of biases is similar to the grouping observed from the dimensionless function discuss in the previous section.

4.8 Conclusions for $H_s^{\max}$ Parameterizations

Presented in this section are the results of the development of maximum wave height response models which incorporated three forms of X_{eq}. The first approach considered the use of dimensionless functions, which produced best-fit curves that can be solved for the prediction of $H_s^{\max}$. This approach yielded RMSE that range between 0.52m – 0.68m. Additionally, the accuracy for this method varied greatly as the highest scatter index was 0.28 for the open-coast points and 0.37 for the bay points. At the shoreline, the variation in the individual biases, gives an indication of how strongly the various forms of the equivalent fetch and the bathymetric depth ultimately determines the predicted $H_s^{\max}$, from the dimensionless functions. Similarly, the grouping in the individual biases in the bay, gives an indication of how strongly the geographical location of the points helps to determine the predicted $H_s^{\max}$. It is observed that the model generally under predicted the $H_s^{\max}$ at points that are located where a buildup of surge occurs.

The second approach uses the SPM method with the inclusion of the three forms of X_{eq}. When compared to the aforementioned dimensionless approach, this method produced a lower RMSE of 0.37m. Additionally, the accuracy for this method was

higher as the lowest scatter index was 0.23 for the open-coast points and 0.31 for the bay points. At both the shoreline and bay points, the equal biases by both X_{eq-Y} and X_{eq-AY} when compared to the biases of X_{eq-A}, gives an indication of how strongly the functional form of the equivalent fetch, as incorporated into the SPM model, determines the $H_s^{\max}$. The range of over-prediction across all the points seem to indicate that geographical location does not play an influence and the wave growth as govern by SPM seem to work well in the bay. One possible reason is that the shallow water forecasting curves, from which the SPM model was derived, contain depth, while the dimensionless forms used in the analysis does not. The only place depth enters into the dimensionless formulations is through the power fit from the ADCIRC-SWAN results.

CHAPTER V

SUMMARY AND CONCLUSIONS

Computational results provided by the coupled ADCIRC-SWAN numerical model indicate that for a range of simulated hurricane landfall locations, central pressures, radius sizes and forward approach speeds, a wide range of spatial and temporal characteristics for the significant wave height are possible. The location of hurricane landfall results in significant differences in the wave height at the specified points. This is due to the spatial variation of the maximum wind velocity vectors that produce elevated surge levels in the near-shore, shoreline and bay area. This subsequently produces different maximum wave heights as water depth plays an important role in the generation of hurricane waves. Additionally, the variation in central pressures, radius sizes and forward speed each play a role in the generation of the maximum wave heights and they produce elevated surge levels that contribute to wave generation. The time evolution trend of the generation of the significant wave height is found to be unique to its geographic location. At the near-shore location the wave height builds up steadily, and the shape of its maximum is somewhat broad over time. At the shoreline, there is a buildup of wave height that ramps up suddenly and also decays suddenly. Finally, the Corpus Christi location appears to have a trend similar to the near-shore location, with the difference that the wave height is zero until the hurricane begins to affect the bay.

The development of $H_s^{\max}$ models is determine by incorporating Young's X_{eq}, Alves's modified version of Young's X_{eq} and Alves's X_{eq} models into (1) dimensionless best-fit equations and (2) SPM model. The dimensionless best-fit equation approach indicates of how strongly the various forms of the equivalent fetch and the bathymetric depth ultimately determines the predicted $H_s^{\max}$. This approach yielded RMSE that range between 0.52m – 0.68m. Additionally, the accuracy for this method varied greatly as the highest scatter index was 0.28 for the open-coast points and 0.37 for the bay points. The SPM approach gives an indication of how strongly the functional form of the equivalent fetch determines the predicted $H_s^{\max}$. When compared to the dimensionless approach, this method produced a lower RMSE of 0.37m. Additionally, the accuracy for this method was higher as the lowest scatter index was 0.23 for the open-coast points and 0.31 for the bay points.

Studying the possible effects of various parameters on wave height and the ability to develop practical tools of estimating the maximum hurricane generated waves is very important. As shown in the literature review, numerical models that focus on these areas are limited. Should hurricanes increase in frequency in the near future, there is an increased risk for damages relating to both storm surge and wave forces. Thus, topics of recommended future research include:

- Evaluating wave height responses to a larger set of hurricane scenarios and the inclusion of additional parameters such as angle of hurricane approach

- Determine the equivalent fetch coefficients and exponents based on the coupled model results of ADCIRC – SWAN
- Field measurements of near-shore and inland wave heights, with surge and wave sensors (Kennedy et al., 2011b), to compare the coupled numerical of ADCIRC – SWAN
- Consider couple model simulations for other areas in the Gulf of Mexico, for example the upper Texas coast or the west coast of Florida, which have different bathymetric and topographic conditions

REFERENCES

Alves, J. H. G. M., Tolman, H. L., and Chao, Y. Y. (2004). "Forecasting Hurricane-Generated Wind Waves At NOAA/NCEP." *JCOMM Tech. Rep. 29*, WMO/TD-No 1319. [polar.ncep.noaa.gov/mmab/papers/tn242/MMAB242.pdf].

Atkinson, J., Westerink, J., Wamsley, T., Cialone, M., Dietrich, C., Dresback, K., Kolar, R., Resio, D., Bender, C., Blanton, B., Bunya, S., de Jong, W., Ebersole, B., Grzegorzewski, A., Jensen, B., Pourtaheri, H., Ratcliff, J., Roberts, H., Smith, J., and Szpilka, C. (2008). "Hurricane Storm Surge and Wave Modeling in Southern Louisiana: A Brief Overview." *Proceedings of the Tenth International Conference on Estuarine and Coastal Modeling*, Newport, RI, 467-506.

Bender, C., Smith, J. M., and Kennedy, A. (2010). "Hurricane Ike (2008) Nearshore Waves: Simulations and Measurements." *32nd International Conference on Coastal Engineering (ICCE)*, Shanghai, China.

Berg, R. (2009). "Tropical Cyclone Report: Hurricane Ike, 1-14 September 2008," National Hurricane Center, Miami FL.

Booij, N., Ris, R. C., and Holthuijsen, L. H. (1999). "A Third-Generation Wave Model for Coastal Regions, 1, Model Description and Validation." *J. Geophys. Res.*, 104(C4), 7649-7666.

Bretschneider, C. L. (1954). “Generation of Wind Waves over a Shallow Bottom.” Beach Erosion Board Technical Memorandum No. 51, U.S. Army Corps of Engineers, Washington, D.C., 24 pp.

Bunya, S., Dietrich, J. C., Westerink, J. J., Ebersole, B. A., Smith, J. M., Atkinson, J. H., Jensen, R., Resio, D. T., Luettich, R. A., Dawson, C., Cardone, V. J., Cox, A. T., Powell, M. D., Westerink, H. J., and Roberts, H.J. (2010). “A High Resolution Coupled Riverine Flow, Tide, Wind, Wind Wave and Storm Surge Model for Southern Louisiana and Mississippi: Part I - Model Development and Validation.” *Monthly Weather Review*, 138(2), 345-377

Cardone, V. J., Greenwood, C. V., and Greenwood, J.A. (1992). “Unified Program For The Specification Of Hurricane Boundary Layer Winds Over Surfaces Of Specified Roughness.” *Contract Report CERC-92-1*, U.S. Army Corps of Engineers, Vicksburg, Miss.

Dean, R. G., and Dalyrmple, R. A. (2002). ‘‘Coastal Processes with Engineering Applications’’ Cambridge University Press, Cambridge.

Dietrich, J.C., Bunya, S., Westerink, J. J., Ebersole, B. A., Smith, J. M., Atkinson, J. H., Jensen, R., Resio, D. T., Luettich, R. A., Dawson, C., Cardone, V. J., Cox, A. T., Powell, M. D., Westerink, H. J., and Roberts, H. J. (2010a). “A High Resolution Coupled Riverine Flow, Tide, Wind, Wind Wave and Storm Surge Model for Southern Louisiana and Mississippi: Part II - Synoptic Description and Analyses of Hurricanes Katrina and Rita.” *Monthly Weather Review*, 138, 378-404.

Dietrich, J.C., Westerink, J. J., Kennedy, A. B., Smith, J. M., Jensen, R., Zijlema, M., Holthuijsen, L. H., Dawson, C. N., Luettich, R. A., Powell, M. D., Cardone, V. J., Cox, A. T., Stone, G.W., Pourtaheri, H., Hope, M. E., Tanaka, S., Westerink, L., Westerink, H., and Cobell, Z. (2010b). "Hurricane Gustav (2008) Waves, Storm Surge and Currents: Hindcast and Synoptic Analysis in Southern Louisiana." *Monthly Weather Review*, 139, 2488-2522.

Dietrich, J.C., Zijlema, M., Westerink, J. J., Holthuijsen, L. H., Dawson, C. N., Luettich, R. A., Jensen, R., Smith, J. M., Stelling, G. S., and Stone, G. W. (2011a). "Modeling Hurricane Waves and Storm Surge using Integrally-Coupled, Scalable Computations." *Coastal Eng*., 58, 45–65, doi:10.1016/j.coastaleng.2010.08.001.

Dietrich, J.C., Tanaka, S., Westerink, J. J., Dawson, C. N., Luettich Jr., R. A., Zijlema, M., Holthuijsen, L. H., Smith, J. M., Westerink, L. G., and Westerink, H. J. (2011b). "Performance of the Unstructured-Mesh, SWAN+ADCIRC Model in Computing Hurricane Waves and Surge." *Journal of Scientific Computing*, doi: 10.1007/s10915-011-9555-6.

Federal Emergency Management Agency (FEMA) (2010a). "Most Expensive Presidentially Declared Disasters." accessed on 15th September 2012. [http://www.mmrs.fema.gov/hazard/hurricane/top10hu.shtm].

Federal Emergency Management Agency (FEMA) (2010b). "Hurricane Hazards: Storm Surge." accessed on 23rd April 2012. [http://www.fema.gov/hazard/hurricane/hu_surge.shtm].

Garratt, J. R. (1977). "Review of Drag Coefficients over Oceans and Continents." *Monthly Weather Review*, 105, 915-929.

Hasselmann, K., Barnett, T. P., Bouws, E., Carlson, H., Cartwright, D. E., Enke, K., Ewing, J. A., Gienapp, H., Hasselmann, D. E., Kruseman, P., Meerburg, A., Muller, P., Olbers, D. J., Richter, K., Sell, W., and Walden, H. (1973). "Measurements of Wind Wave Growth and Swell Decay during the Joint North Sea Wave Project (JONSWAP)." *Deutsch. Hydrogr. Z.*, Suppl., A8, 12, 95 pp.

Holland, G. J. (1980). "An Analytic Model of the Wind and Pressure Profiles in Hurricanes." *Monthly Weather Review*, 108(80), 1212-1218.

Holthuijsen, L. H. (2007). "Waves in Oceanic and Coastal Waters," Cambridge University Press, Cambridge, UK.

Irish, J. L., and Resio, D. T. (2009). "A hydrodynamic based surge scale for hurricanes." *Ocean Engineering*, 37 (2010), 69-81.

Kennedy, A., Rogers, S., Sallenger, A., Gravois, U., Zachry, B., Dosa, M., and Zarama, F. (2011a). "Building Destruction from Waves and Surge on the Bolivar Peninsula during Hurricane Ike." *Journal of Waterways, Port, Coastal, and Ocean Engineering*, May/June 2011, 132-141.

Kennedy, A., Gravois, U., and Zachry, B. (2011b). "Observations of Landfalling Wave Spectra during Hurricane Ike." *Journal of Waterways, Port, Coastal, and Ocean Engineering*, V. 137, May/June 2011, 142-145.

Kennedy, A. B., Gravois, U., Zachry, B., Westerink, J. J., Hope, M. E., Dietrich, J. C., Powell, M. D., Cox, A. T., Luettich Jr., R. A., and Green, R. G. (2011c). "Origin

of the Hurricane Ike forerunner surge." *Geophys. Res. Lett., 38,* L08608, doi:10.1029/2011GL047090.

King, D. B., and Shemdin, O. H. (1978). "Radar Observations of Hurricane Wave Directions." *16th International Conference on Coastal Engineering (ICCE),* Hamburg, Germany, 209-226.

Knabb, R. D., Rhome, J. R., and Brown, D. P. (2005). "Tropical Cyclone Report: Hurricane Katrina, 23-30 August 2005," National Hurricane Center, Miami FL.

Kraus, N. C., and Lin, L. (2009). "Hurricane Ike along the upper Texas coast: An introduction," *Shore & Beach,* 77(2).

Kumar, V. S., Mandal, S., and Kumar, K. A. (2003). "Estimation of wind speed and wave height during cyclones." *Ocean Engineering*, 30 (2003), 2239-2253.

Luettich, R. A., Westerink, J. J., and Scheffner, N. W. (1991). "ADCIRC: An Advanced Three-Dimensional Circulation Model For Shelves, Coasts, And Estuaries: Report 1: Theory and Methodology of ADCIRC-2DDI and ADCIRC-3DL." *Technical Report DRP-92-6*, US Army Corps of Engineers, Washington, DC.

Luettich, R. A., and Westerink, J. J. (2004). "Formulation and Numerical Implementation of the 2D/3D ADCIRC Finite Element Model version 44.XX." web publication. [http://adcirc.org/adcirc_theory_2004_12_08.pdf].

Lynch, D. R., and Gray, W. G. (1979). "A Wave Equation Model For Finite Element Tidal Computations." *Comput. Fluids 7, 207-228.*

Massel, S. R. (1996). "Ocean Surface Waves: Their Physics And Prediction." World Scientific Publishing Co. Pte. Ltd., Singapore.

National Oceanic and Atmospheric Administration (2012). "The Great Galveston Hurricane of 1900." accessed on 15th September 2012. [http://celebrating200years.noaa.gov/magazine/galv_hurricane/welcome.html].

National Oceanic and Atmospheric Administration – National Hurricane Center (NOAA-NHC) (2012a). "National Hurricane Center – Hurricanes in History." accessed on 15th September, 2012. [http://www.nhc.noaa.gov/outreach/history/#top].

National Oceanic and Atmospheric Administration – National Hurricane Center (NOAA-NHC) (2012b). "National Hurricane Center – Storm Surge Overview." accessed on 15th September, 2012. [http://www.nhc.noaa.gov/surge/#EVENTS].

Padgett, J., DesRoches, R., Nielson, B., Yashinsky, M., Kwon, O. S., Burdette, N., and Tavera, E. (2008). "Bridge Damage and Repair Cost from Hurricane Katrina." *Journal of Bridge Engineering*, 13(1), 6-14.

Panigrahi, J. K. and Misra, S.K. (2010). "Numerical hindcast of extreme waves." *Nat Hazards*, (2010) 53:361-374, doi: 10.1007/s11069-009-9438-4.

Ris, R. C., Holthuijsen, L. H. and Booij, N. (1999). "A Third-Generation Wave Model for Coastal Regions, 2, Verification." *J. Geophys. Res.*, 104, C4, 7667-7681.

Sheppard, D. M., Slinn, D. N., and Hagen, S., (2007). "Design Hurricane Storm Surge Study, Final Report." Florida Department of Transportation. 149 pgs.

Sorensen, R.M. (1993). "Basic Wave Mechanics for Coastal and Ocean Engineers." John Wiley, NY.

Texas A & M Supercomputing Facility (2012). [http://sc.tamu.edu/].

Thompson, E. F., and Cardone, V. J. (1996). "Practical Modeling of Hurricane Surface Wind Fields." *Journal of Waterways, Port, Coastal, and Ocean Engineering*, American Society of Civil Engineers, July/August 1996, pp.198-205.

U.S. Army Coastal Engineering Research Center (1984). "Shore Protection Manual, 4th Edition." U.S. Government Printing Office, Washington, DC.

U.S. Army Corps of Engineers (USACE) (2008). "Flood Insurance Study: Southeastern parishes, Louisiana—Intermediate Submission 2: Offshore water levels and waves." U.S. Army Corps of Engineers, New Orleans District, 235 pp.

U.S. Army Corps of Engineers (USACE) (2011). "Flood Insurance Study: Coastal Counties, Texas—Intermediate Submission 2: Scoping and Data Review." U.S. Army Corps of Engineers, New Orleans District, 182 pp.

Vickery, P. J., Skerlj, P. F., Steckley, A. C., and Twisdale, L. A. (2000). "Hurricane Wind Field Model for use in Hurricane Simulations." *Journal of Structural Engineering*, American Society of Civil Engineers, Vol. 126, No. 10, October 2000, 1203-1221.

Weisberg, R. H., and Zheng, L. (2006). "A Simulation of the Hurricane Charley Storm Surge and its breach of North Captiva Island." *Florida Scientist*, 69, 152-165.

Westerink, J. J., Luettich, R. A., and Muccino, J. C. (1994). "Modeling tides in the western North Atlantic using unstructured graded grids." *Tellus*, 46A. 178-199.

Westerink, J. J., Luettich, R. A., Feyen, J. C., Atkinson, J. H., Dawson, C., Roberts, H. J., Powell, M. D., Dunion, J. P., Kubatko, E. J., and Pourtaheri, H. (2008). "A Basin- to Channel-Scale Unstructured Grid Hurricane Storm Surge Model Applied to Southern Louisiana." *Monthly Weather Review*, 136, March 2008, 833-864.

World Meteorological Organization (WMO) (1998). "Guide to Wave Analysis and Forecasting, 2nd Edition." WMO No.702, Geneva, Switzerland.

Wu, C. W., Taylor, A. T., Chen, J., and Shaffer, W. (2003). "Tropical Cyclone Forcing of Ocean Waves." *Fifth Conference on Coastal Atmospheric and Ocean Prediction and Processes*, Seattle, WA, pp 62-64.

Young, I. R. (1988). ''Parametric Hurricane Wave Prediction Model.'' *Journal, Waterway, Port, Coastal and Ocean Engineering Division*, American Society of Civil Engineers, September, 114, pp. 637–652.

Young, I. R. (1999). ''Wind Generated Ocean Waves.'' Amsterdam, Elsevier, 288pp.

Young, I. R. (2003). ''A review of the sea state generated by hurricanes.'' *Marine Structures*, 16 (2003), pp. 201-218.

Zijlema, M., (2010). "Computation of wind–wave spectra in coastal waters with SWAN on unstructured grids." *Coastal Engineering* 57, 267–277.